

Representation of the tropical intraseasonal variability and its impact on seasonal predictability in a multi-model ensemble

Prince K. Xavier⁽¹⁾, Jean-Philippe Duvel⁽¹⁾,
Francisco J. Doblas-Reyes⁽²⁾

Research Department

⁽¹⁾ Laboratoire de Météorologie Dynamique, Ecole Normale Supérieure, Paris, France

⁽²⁾ European Centre for Medium-Range Weather Forecasting, Reading, UK

April 2007

This paper has not been published and should be regarded as an Internal Report from ECMWF.
Permission to quote from it should be obtained from the ECMWF.



European Centre for Medium-Range Weather Forecasts
Europäisches Zentrum für mittelfristige Wettervorhersage
Centre européen pour les prévisions météorologiques à moyen

Series: ECMWF Technical Memoranda

A full list of ECMWF Publications can be found on our web site under:
<http://www.ecmwf.int/publications/>

Contact: library@ecmwf.int

© Copyright 2007

*European Centre for Medium Range Weather Forecasts
Shinfield Park, Reading, Berkshire RG2 9AX, England*

Literary and scientific copyrights belong to ECMWF and are reserved in all countries. This publication is not to be reprinted or translated in whole or in part without the written permission of the Director. Appropriate non-commercial use will normally be granted under the condition that reference is made to ECMWF.

The information within this publication is given in good faith and considered to be true, but ECMWF accepts no liability for error, omission and for loss or damage arising from its use.

Abstract:

The intraseasonal variability associated with the Asian summer monsoon as simulated by seven coupled general circulation models (CGCMs) are analyzed and validated against observations. The model hindcasts are produced by the DEMETER project. Each hindcast is an integration of six months starting from 1 February, 1 May, 1 August and 1 November and comprises an ensemble of nine members. All seven models have been run for a common period of 1980–2001. The focus is on the spatial and seasonal variations associated with the summer monsoon intraseasonal oscillations (ISO) of outgoing longwave radiation (OLR), their large-scale organization, propagation characteristics, the air-sea coupling, their deterministic predictability and implications on seasonal predictability.

A multi-variate Local Mode Analysis (LMA, essentially a complex EOF analysis over a window of 90 days moving over the 180 days of hindcasts) has been utilized in order to evaluate the above characteristics of ISOs in the hindcasts against observations. Most models have problems in simulating large-scale organized perturbations of the convection. In addition, perturbation patterns are more variable from one intraseasonal event to another compared to observation. However, most models do exhibit some form of northeastward propagation of the perturbations over the Indian Ocean. Realistic periods of the modes (25–35 days) are produced in a few models, while most models produce shorter periods (20–25 days). Models with poor seasonal cycle tends to have larger biases in the northeastward propagation and organization. One possible source of deficiency in organizing intraseasonal large-scale convective perturbation could be the air-sea interaction. The analysis of the nature of coupling in the hindcasts indeed shows that most models simulate too weak SST perturbations and systematic phase quadrature between OLR and SST, indicative of a slab-ocean-like response of the temperature to surface flux perturbations. Simulation done with the same AGCM and different OGCMs tend to have similar biases of the simulated ISOs, indicative of the importance of atmospheric processes in defining the nature of the intraseasonal SST perturbation. Mainly because of their relatively coarse vertical resolution, the different OGCMs used are however limited in their ability to represent intraseasonal processes, such as warm layer formation, which are important for realistic simulation of the SST perturbation and feedback at intraseasonal time-scales. This may explain the too small SST amplitude and the relatively similar behavior for the different OGCMs.

Evaluation of the predictability at the ISO time scale (10–50 days) is also performed on the basis of pentad mean OLR maps. Results show a better predictability in the summer (1 May initial conditions) hindcasts compared to the winter hindcasts (1 November initial conditions). This is possibly due to the better predictions and consistency among all ensemble members of the strong seasonal cycle and the embedded ISOs in summer compared to the weaker seasonal cycle in winter. Other intraseasonal and seasonal predictability studies are also presented with an emphasis on the influence of large-scale organized ISO perturbations on the regional seasonal evolution of the precipitation at particular location.

1. Introduction

The intraseasonal variability (ISV: 20 to 90 days) of the tropical convection plays a significant role in the regional distribution of the rainfall in monsoon regions (Fennassy and Shukla 1994, Ferranti et al, 1997, Goswami and Ajayamohan 2001, Goswami and Xavier, 2005). The ISV is associated with low-level wind perturbations near the equator that can also play a role in triggering El Niño events (e.g. McPhaden 1999; Lengaigne et al. 2002). Current problems in simulating and predicting the seasonal mean and interannual variations may be thus related in part to shortcomings of ISV simulations in GCMs.

The ISV indeed remains a phenomenon difficult to simulate in current forced or coupled Global Circulation Models (GCMs). These difficulties were pointed out by previous studies such as Slingo et al (1996) that examined the ISV in 15 atmospheric GCMs (AGCM) participating in the Atmospheric Model Intercomparison Project (AMIP). The focus of their study was on the northern hemisphere (NH) winter

variability related in part to the Madden Julian Oscillation (MJO, Madden and Julian 1994, Zhang 2005). The conclusions were that most atmospheric GCMs (AGCM) have difficulty in properly simulating the MJO in terms of strength, propagation speed, seasonality and interannual variability. The results of their analysis also suggested that models that simulate realistic basic states, including the annual cycle and basic relationships between warm sea surface temperatures (SST) and precipitation rate, tend to have better MJO simulations. Another study by Sperber et al (2001), while focussing on the dynamical seasonal prediction of the summer monsoon, assessed how well the intraseasonal variability is represented in the models. Their results showed that for many models, the dominant dynamical pattern of subseasonal variability is often simulated. However, the AGCMs had difficulty in representing the spatial perturbation patterns of the intraseasonal oscillations. Kang et al (2002) examined how well forced atmospheric GCMs simulate the intraseasonal variation of the Asian summer monsoon and showed that the simulated northward propagation of intraseasonal perturbations of precipitation occur 20-30 days earlier than in the observations. This result is in partial agreement with the case study of Wu et al. (2002) that indicated that the simulated and observed oscillations are approximately in quadrature. This is due to the too fast response of the convection to SST perturbations in the forced AGCM. In another study, the ISV of the Asian summer monsoon was analysed by Waliser et al (2003a) using data from 10 GCMs participating in the CLIVAR/Asian-Australian Monsoon Panel. The results showed that the fidelity of a model to represent the area averaged intraseasonal variance in summer and winter are strongly linked. Compared to observations, the simulated intraseasonal oscillations (ISO) were found to be less coherent; they also lacked sufficient eastward propagation, and had reduced zonal and meridional extensions. They also found the (statistically expected) positive relationship between the strength of the simulated ISV and the spread of the seasonal mean (i.e. inter-member variability in the ensemble forecast). Zhang et al (2006) evaluated the numerical simulation of the MJO by four pairs of coupled and uncoupled GCMs and found that the air-sea coupling generally enhances the simulated eastward propagating signal. However its effect on the phase relationships and coherence between precipitation and low level winds, their geographical distributions, seasonal cycles and interannual variability was shown to be inconsistent among the simulations. Some of these biases in the simulated MJO were shown to be related to the biases in the background state of the mean precipitation, low level winds and boundary layer moisture convergence.

Part of the deficiency of the AGCMs to represent the ISV may be related to the representation of air sea interaction at these timescales. Observations show indeed strong perturbations of the SST associated to intraseasonal events that may have significant impact on the triggering and the evolution of intraseasonal events (Sengupta et al 2001, Vecchi and Harrison 2002, Bhat et al 2001, Webster et al 2002, Sengupta and Ravichandran 2001, Waliser et al 2003b). For this process, the depth of the ocean mixed layer is an important factor that determines at the same time its reactivity and its heat content (Maloney and Sobel 2004, Bellenger and Duvel 2007). The variation of the temperature of the ocean mixed layer is due in part to fluctuations of the net heat flux at the surface caused by intraseasonal perturbations of cloudiness and surface winds. Other physical sources may however also contribute to the ISV of this temperature, such as the mixing with deeper layers caused by the deepening of the mixed layer (Duvel et al 2004, Duvel and Vialard 2006). Also the formation of surface warm layers may contribute to increase the SST during low-wind phases of the intraseasonal events, contributing to amplify the amplitude of the intraseasonal perturbation of the SST. Some of these processes, such as the warm layer formation, are not or are insufficiently taken into account in current coupled GCM, mainly because of the relatively coarse vertical resolution of the ocean model (Woolnough et al, 2007). However, simulations done with coupled instead of forced GCMs may

result in more realistic ISV amplitude, propagation characteristics and phase relationship between atmospheric and oceanic parameters (Kemball-Cook and Wang 2001, Fu et al 2003). Improvements given by the coupling with the ocean may in turn result in improved predictability of the ISV (Fu et al 2007). Hindcasts (i.e. a posteriori forecasts) of a few months based on coupled GCMs are then expected to produce more realistic ISV than their atmosphere only counterparts in terms of large scale organization, period, phase propagation, phase relationship between convection and SST, etc. However, biases in the ISV are also expected for these hindcasts and an objective assessment to identify these biases and their possible causes could help to rectify them and improve the simulations. One objective of this study is thus to assess the representation of the ISV in the hindcasts. Also, the representation of the subseasonal variability is important for the seasonal forecasts of the monsoon. A good representation of this subseasonal variability will be especially important to improve the seasonal forecast for specific regions and not only for very integrated indices such as the All Indian Rainfall (AIR). There is indeed a strong need for such regional subseasonal forecasts of the monsoon precipitation (Webster and Hoyos, 2004).

In this study, we first develop an approach to evaluate the simulation of the ISV in a series of hindcasts produced by an ensemble of coupled GCMs with an emphasis on the coupling with the ocean at intraseasonal timescale. To this end, an original approach is developed that makes it possible to compare statistically two ensembles of observed and simulated intraseasonal events. This approach is based of the Local Mode Analysis (LMA) introduced by Goulet and Duvel (2000) and further developed in a multivariate approach by Duvel and Vialard (2007). This multivariate approach is used here to extract SST and surface wind speed (SWS) perturbations related specifically to large-scale organized convective perturbations. This report describes this approach and illustrates it by an application on the DEMETER hindcast ensemble (Palmer et al, 2004) for NH summer and winter using 7 AGCMs coupled to full ocean models.

Section 2 presents the details of DEMETER hindcasts and the LMA approach used to extract the large scale organized intraseasonal convective perturbations and the associated variability in other fields (SST and SWS). The model evaluation in terms of the seasonal mean climate and the climatological 20-90 days intraseasonal variance for the NH summer hindcasts are described in Section 3. Section 4 evaluates the organized ISV in the hindcasts using the multivariate LMA. In order to analyze the role of the coupling in the representation of the ISV, a particular emphasis is put on the phase relationships between OLR, SST and SWS. A detailed comparison of the periods, degree of organization and the reproducibility of the intraseasonal modes in the models are assessed against the observations and contrasted between summer and winter. The 20-50 day predictability for summer and winter hindcasts is examined in Section 5 and the seasonal predictability of the intraseasonal activity over a given basin is studied in Section 6. Section 7 presents the main conclusions of this analysis.

2. Data and analysis

2.1. Models and data sets

DEMETER is the acronym of the European project entitled “Development of a European Multimodel Ensemble system for seasonal to inTERannual prediction” (Palmer et al, 2004). Components of each model are given in Table 1.

For each model (except for SMPI) the uncertainties in the initial conditions are represented through an ensemble of nine different ocean initial conditions. This is achieved by creating three different ocean analyses; a control ocean analysis forced with momentum, heat and mass flux from the ECMWF Reanalysis (ERA40) and two perturbed ocean analyses created by adding wind stress perturbations to the ERA40 momentum fluxes. The wind stress perturbations are randomly taken from a set of monthly differences between two quasi-independent analyses. In addition, in order to represent the uncertainties in SSTs, four SST perturbations are added and subtracted at the start of the hindcasts. The atmospheric and land surface initial conditions are taken from the ERA40 data set. An alternative coupled initialization method has been used for SMPI. Ocean observations have been assimilated only in the UKMO run after 1987. The DEMETER hindcasts starts from 1 February, 1 May, 1 August or 1 November. Each hindcast is an ensemble of nine integrations (nine members) of six months. All seven models have been run for a common period of 1980-2001, although some of the models have been integrated over an even longer period (1958-2001). In this study, the common period 1980-2001 is used in order to facilitate comparison between models.

Table 1: Seven comprehensive European global coupled atmosphere-ocean models are installed at European Centre for Medium-Range Weather Forecasts (ECMWF). They are abbreviated as CNRM (Centre National de Recherche en Météorologie), CRFC (European Centre for Research and Advanced Training in Scientific Computation, France; CERFACS), LODY (Laboratoire d'Océanographie Dynamique et de Climatologie, France; LODYC), SCNR (National Institute for Geophysics, Italy; INGV), SCWC (ECMWF), SMPI (Max-Planck Institute für Meteorologie, Germany; MPI) and UKMO (Meteorological Office, UK).

Model Name	Atmospheric component			Oceanic component		
	Model	Resolution	Initial condition	Model	Resolution	Initial condition
CNRM	ARPEGE	T63L31	ERA40	OPA 8.1	2 x 1.5 (0.5 Eq). 31 levels	Ocean analysis forced by ERA40
CRFC	ARPEGE	T63L31	ERA40	OPA 8.2	2x2 31 levels	Ocean analysis forced by ERA40
LODY	IFS	T95L40	ERA40	OPA 8.2	2x2 31 levels	Ocean analysis forced by ERA40
SCNR	ECHAM4	T42 L19	Coupled AMIP type run	OPA 8.1	2 x 1.5 (0.5 Eq) 31 levels	Ocean analysis forced by ERA40
SCWC	IFS	T95L40	ERA40	HOPE-E	1.4x1.4 (0.3Eq), 29 levels	Ocean analysis forced by ERA40
SMPI	ECHAM5	T42L19	Coupled run relaxed to observed SST	MPI-OM1	2.5x2.5 (0.5Eq), 23 levels	Coupled run relaxed to observed SST
UKMO	HadCM3	2.5x3.75, L19	ERA40	GloSea OGCM, HadCM3 based	1.25x1.25(0.3Eq), 40 levels	Ocean analysis forced by ERA40

CNRM and CRFC uses the same AGCM (ARPEGE) and so do LODY and SCWC (ECMWF IFC), but with different Ocean GCMs (OGCMs). The same version of OPA (8.1) is coupled with ARPEGE and ECHAM4 in the CNRM and SCNR respectively. Version 8.2 of OPA is common for CRFC and LODY. These pairs of models may be used to account for the relative importance of the atmospheric or oceanic processes in the simulated ISV. For example, comparison between LODY and SCWC may provide information on the

importance of atmospheric processes in the models, while a comparison between CRFC and LODY may be helpful in understanding the role of oceanic processes in the hindcasts.

This study will compare and contrast the major features of intraseasonal variability in OLR (a reliable observable quantity used as a proxy for deep convection), and the associated variability in surface winds (at 10 m) and SST in the hindcasts starting from 1 May and 1 November for the period 1980-2001. NOAA interpolated OLR (Liebmann and Smith, 1996) and surface winds and SST from ERA-40 reanalysis are used as reference observations. SST data provided by ERA-40 (same as Reynolds and Smith, 1994) is weekly averaged and is known to underestimate the intraseasonal variance by a factor of 2 for certain regions and seasons (Duvel and Vialard, 2007). The spatial patterns of variability of this SST nevertheless show similarity with that of the TMI SST (Wentz et al 2000). TMI is not used here since it is available since the end of 1997 only. With the caution on the reported underestimation of the amplitude of intraseasonal SST fluctuations (Duvel and Vialard 2007), we thus use ERA-40/Reynolds SST to compare with the hindcasts, as this is the only available dataset that spans the entire period considered. Hereafter, hindcasts starting from 1 May and 1 November will be referred to as summer and winter hindcasts respectively (in reference to the northern hemisphere).

2.2. The local mode analysis (LMA)

Spatial patterns and the temporal characteristics of the intraseasonal convective events are determined using the Local Mode Analysis (LMA; Goulet and Duvel 2000). We use this technique because of the intermittency of the intraseasonal variability. The LMA makes it possible to detect and characterize in a simple mathematical form the main events of an intermittent phenomenon that succeed one another in time. In addition, the LMA gives a pattern for each intraseasonal event. This allows comparing not only average modes but also the distribution of the patterns.

This section is an adaptation of the description of the LMA technique reported in Duvel and Vialard (2007).

2.2.1. Computation of the local modes for one parameter

The LMA technique is based on a CEOF computation on a running time section (of 90 days here). For each time step (m) of the running analysis, only the *leading CEOF* is retained, corresponding to one particular pattern $\tilde{Z}_p^m(x)$ explaining a percentage of variance Π_p^m . Maxima in the Π_p^m time series are then identified and the *leading CEOF* of the time section corresponding to these maxima are called *Local Modes*. One can demonstrate that the spatial patterns $\tilde{Z}_p^m(x)$ of these *Local Modes* are more persistent in time and/or more spatially coherent than the patterns of other *leading CEOF* (Goulet and Duvel 2000).

Mathematically, for each time step (m), we consider the 90-day time series $S_p^m(x, t)$ of parameter (p), for each region (x) with $1 \leq x \leq N$ and $1 \leq t \leq T$ ($T=90$). The leading eigenvector is computed from the cross spectrum matrix $\tilde{\zeta}_p^m$ defined as:

$$\tilde{\zeta}_p^m(k, k') = \sum_{x=1}^N \tilde{F}_p^m(x, k) \tilde{F}_p^{m*}(x, k') \quad (1)$$

where \tilde{X} are complex numbers and \tilde{X}^* their complex conjugate, k is the harmonic number (for the whole spectrum $1 \leq k \leq T/2$) and $\tilde{F}_p^m(x, k)$ represents the Fourier coefficients defined as:

$$\tilde{F}_p^m(x, k) = \frac{\sqrt{2}}{T} \sum_{t=1}^T w(t) S_p^m(x, t) e^{-2i\pi kt/T} \quad (2)$$

where $w(t)$ is the Welch window. Since the Complex EOF has to be applied to a restricted time-spectral domain, $S_p(x, t)$ is filtered prior to the analysis and $\tilde{\zeta}_p^m$ can be computed on a restricted time-spectral band $[k_1, k_2]$ so that the dimension of the matrix is only $K_n \times K_n$ with $K_n = k_2 - k_1 + 1$. The leading eigenvectors of $\tilde{\zeta}_p^m$ is a complex normalized spectrum $\tilde{\psi}_p^m(k)$ from which we can retrieve the spatial eigenvectors $\tilde{Z}_p^m(x)$ by:

$$\tilde{Z}_p^m(x) = \sum_{k=k_1}^{k_2} \tilde{F}_p^m(x, k) \tilde{\psi}_p^m(k) \quad (3)$$

For a region x , the reconstructed time series associated with the local mode of the time step (m) is given by:

$$S_p^m(x, t) = A_p^m(x) B^m(t) \cos(\phi_p^m(x) + \chi^m(t)) \quad (4)$$

where $A_p^m(x) = |\tilde{Z}_p^m(x)|$ and $\phi_p^m(x) = \text{Arg}[\tilde{Z}_p^m(x)]$ are respectively the regional standard deviation and phase of the leading complex eigenvector $\tilde{Z}_p^m(x)$. $B^m(t)$ and $\chi^m(t)$ represent respectively the amplitude and phase obtained by inverse Fourier transform of $\tilde{\psi}_p^m(k)$. The summation of $A_p^m(x)^2$ over all regions is the variance of the leading CEOF. It is possible to define a Regional Representation Index $R_p^m(x)$ for the local mode m as:

$$R_p^m(x) = \frac{A_p^m(x)^2}{V_p^m(x)} \quad (5)$$

where,

$$V_p^m(x) = \sum_{k=k_1}^{k_2} \tilde{F}_p^m(x, k) \tilde{F}_p^m(x, k)^* \quad (6)$$

is the variance (weighted by the Welch window) of parameter (p) in the selected frequency band $[k_1, k_2]$. $R_p^m(x)$ represents for each region and the corresponding Local Mode the part of the regional intraseasonal perturbation that is coherent at large scale. Note that the percentage of variance is also given by:

$$\Pi_p^m = \frac{\sum_{x=1}^N A_p^m(x)^2}{\sum_{x=1}^N V_p^m(x)} \quad (7)$$

2.2.2. Multivariate analysis

This technique may be further used to study perturbations of a second parameter (q) associated with the perturbation of the leading parameter (p). Indeed, the projection (Eq.3) of the normalized spectrum $\tilde{\psi}_p^m(k)$ may be done with the Fourier coefficient $\tilde{F}_q^m(x, k)$ of another parameter (q). In such a case, the obtained $\tilde{Z}_{p,q}^m(x)$ represents the spatial pattern of the perturbation of (q) related to the large-scale organized perturbation of (p), through a “spectral key” $\tilde{\psi}_p^m(k)$. In other words, the distribution of amplitudes and phases of $\tilde{Z}_{p,q}^m(x)$ represents the part of the regional signal of (q) that is correlated with the large-scale organized perturbation of (p) represented by the Local Mode (m). As for the reference parameter (p), a Regional Representation Indexes $R_{p,q}^m(x)$ may be defined as

$$R_{p,q}^m(x) = \frac{A_{p,q}^{m^2}(x)}{V_q^m(x)} \quad (8)$$

2.2.3. Average multivariate patterns

The average pattern is computed for the reference parameter from a cross spectrum matrix of dimension (N, N) where N is the number of regions, as described in Goulet and Duvel (2000). Each element of the matrix is an average cross spectrum computed from a given selection (an ensemble S) of Local Modes. For the present study, p is the OLR and the ensemble S is a particular season. This selection may be based on season or on another criterion. Each element of this mean cross spectrum matrix $\bar{\zeta}_{p,s}$ is defined as:

$$\bar{\zeta}_{p,s}(x, x') = \sum_{m \in S} \sum_{k=k_1}^{k_2} \tilde{L}_p^m(x, k) \tilde{L}_p^{m*}(x', k) \quad (9)$$

where $\tilde{L}_p^m(x, k)$ is the spectrum for the parameter p and region x, corresponding to the Local Mode m:

$$\tilde{L}_p^m(x, k) = \tilde{Z}_p^m(x) \tilde{\psi}_p^m(k) \quad (10)$$

Note that the pattern obtained is generally very close (but the percentage of variance is smaller) if one uses the original spectra $\tilde{F}_p^m(x, k)$ instead of the Local Mode spectra $\tilde{L}_p^m(x, k)$. Using the normalized first eigenvector $\tilde{Z}_{p,s}(x)$ of the average cross-spectrum matrix $\bar{\zeta}_{p,s}$, and the regional spectra $\tilde{L}_p^m(x, k)$ (or $\tilde{F}_p^m(x, k)$), the average spectrum $\tilde{\psi}_p^y(k)$ for each Local Mode window (m) is given by:

$$\tilde{\psi}_{p,s}^m(k) = \sum_x \tilde{F}_p^m(x, k) \tilde{Z}_{p,s}^*(x) \quad (11)$$

These spectra are then normalized such that:

$$\sum_{m \in S} \sum_{k=k_1}^{k_2} |\tilde{\psi}_{p,s}^m(k)|^2 = 1 \quad (12)$$

Then, for each parameter q , an average pattern corresponding to these spectra (that are spectral keys corresponding to the average pattern of the reference parameter) can be computed from the spectra $\tilde{L}_q^m(x, k)$ (or $\tilde{F}_q^m(x, k)$):

$$\tilde{Z}_{q,s}^p(x) = \sum_{m \in S} \sum_{k=k_1}^{k_2} \tilde{L}_q^m(x, k) \tilde{\psi}_{p,s}^{m*}(k) \quad (13)$$

These are the average patterns of the perturbation of the parameter q associated to the *large-scale organized perturbations of the reference parameter p* (one may verify that $\tilde{Z}_{p,s}^p(x) = \tilde{Z}_{p,s}(x)$). These patterns are used in section 4 to analyse the average relation between the OLR, the SST and the surface wind intraseasonal perturbations. Since the normalized spectra $\tilde{\psi}_{p,s}^m(k)$ are not from parameter q , the principal component time series corresponding to $\tilde{Z}_{q,s}^p(x)$ and the corresponding variance (and percentage of variance) has to be computed by a projection of the $\tilde{L}_q^m(x, k)$ (or $\tilde{F}_q^m(x, k)$) on $\tilde{Z}_{q,s}^p(x)$.

The LMA makes it possible to measure the resemblance between an average pattern and the patterns for each Local Mode. This is very important to verify if this average pattern is only a mathematical object or if it is representative of the different events, i.e. if it is appropriate to give a physical interpretation of the average pattern. As in Goulet and Duvel (2000), this resemblance is computed as a normalized distance between the complex eigenvectors representing the average pattern $\tilde{Z}_{q,s}^p(x)$ and the pattern of each Local Mode $\tilde{Z}_q^m(x)$. A normalized distance of 0 means that the patterns are identical and a normalized distance of one means that the two patterns are orthogonal.

3. Evaluation of the models' climatology

3.1. Summer mean climatology

The average summer monsoon from model simulations varies in more dimensions (9 members) than in the observations. The averaging on the 9 members will smooth out the statistical residual in the mean due to the stochastic intraseasonal variability. However, since the observed climatology is constructed with a relatively large sample (22 years), this statistical residual is also small and the climatologies are directly comparable. The climatological average OLR, SST and surface winds from the summer hindcasts (May to September) are shown on Fig. 1 and Fig. 2. A general problem endemic to most models (except SMPI) is the OLR minimum does not extend north of 20°N as in observations and the OLR values over Indian subcontinent are larger than in the observations (Fig. 1), the convective perturbation is thus too small. The narrow Inter Tropical Convergence Zone (ITCZ) in LODY and SCWC indicates that the intraseasonal variations in these two models may be limited within this narrow band. The small average OLR in SMPI is also associated to larger precipitation (see www.ecmwf.int/research/demeter).

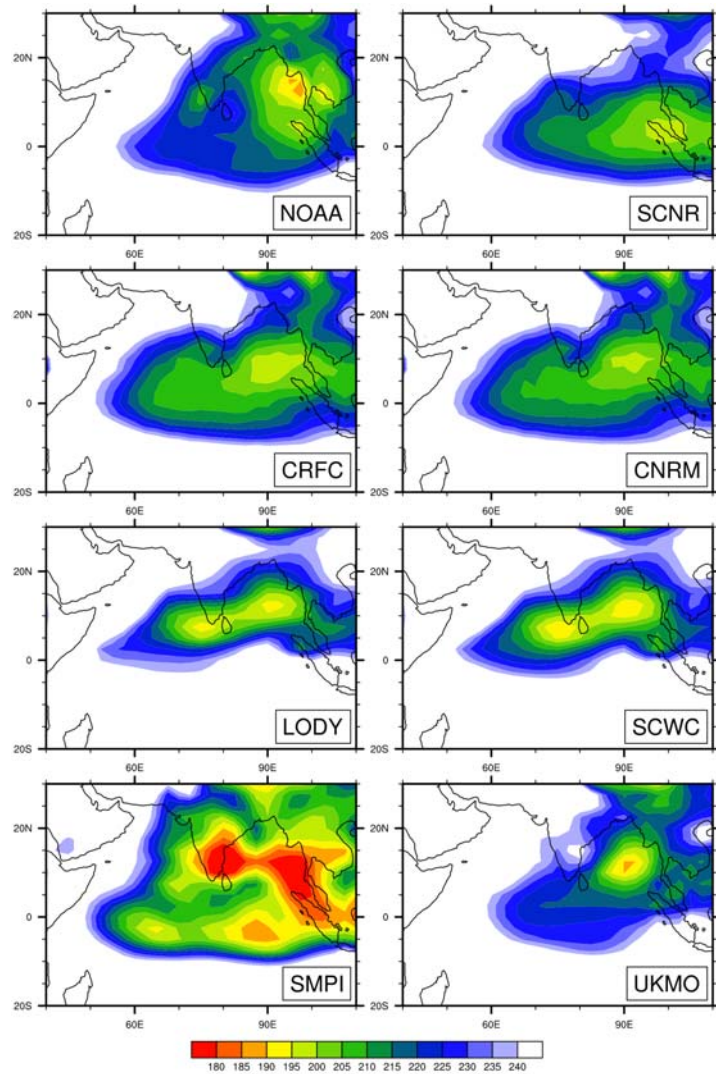


Figure 1: Average (May to September 1980-2001) OLR from observations and the different models. The model's average is computed over the 9 members and the 22 hindcast years. Values are in W m^{-2} .

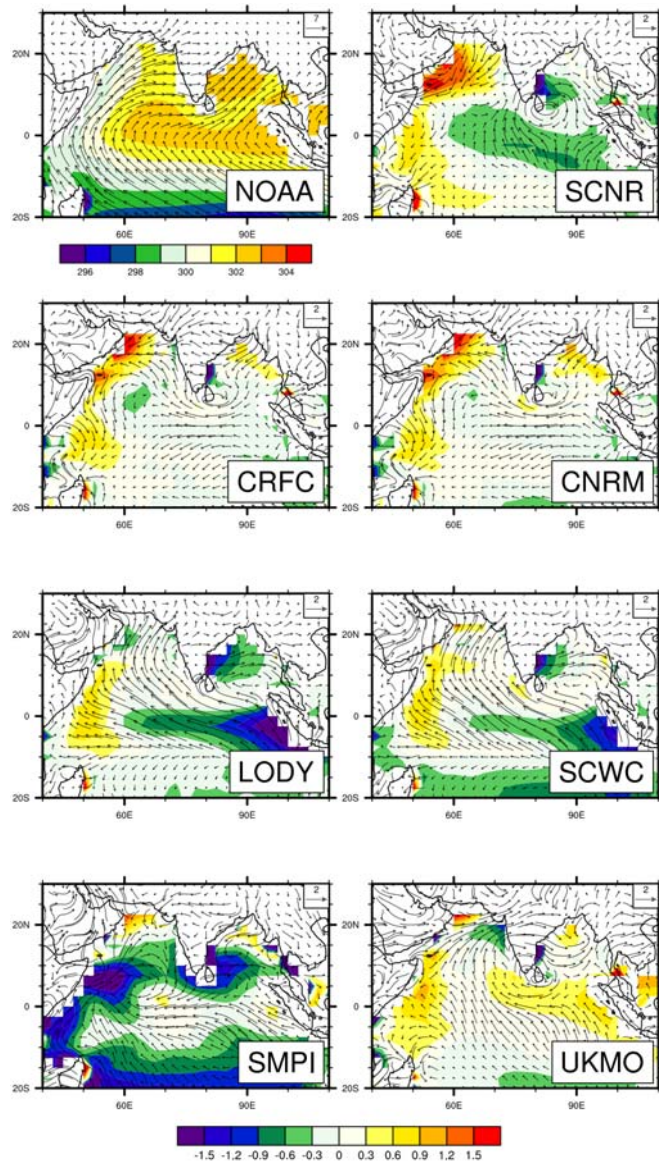


Figure 2: Average (May to September 1980-2001) SST (K) and surface winds ($m s^{-1}$) from ERA40 reanalysis (top left panel). Other panels are the bias for each models (model minus observations). The model's average is computed over the 9 members and the 22 hindcast years.

Surface winds anomalies (model minus observations, Fig. 2) of all models (except SMPI) exhibit an anticyclonic vorticity close to Sri Lanka with an alongshore component on the southeastern coast of India consistent with colder SSTs due to upwelling. SCNR, CRFC and CNRM have weaker low level monsoon flow in the Arabian Sea and associated warmer SST, possibly due to the south-westward alongshore wind anomalies along the coasts of Somalia and Arabia that suppress coastal upwelling during the monsoon season. Enhancement of cross equatorial flow in LODY and SCWC causes strong equatorial upwelling in the eastern equatorial Indian Ocean. The two different ocean models for LODY (OPA 8.2) and SCWC (HOPE) give very similar SST biases, illustrating the expected primary role of the atmospheric forcing in driving SST. By comparison, an hypothetical SST induced atmospheric bias appears to be small, as shown by the large differences between CRFC and LODY (same ocean model.) The large scale cooling of SMPI along the Somalia coast may be related to upwelling.

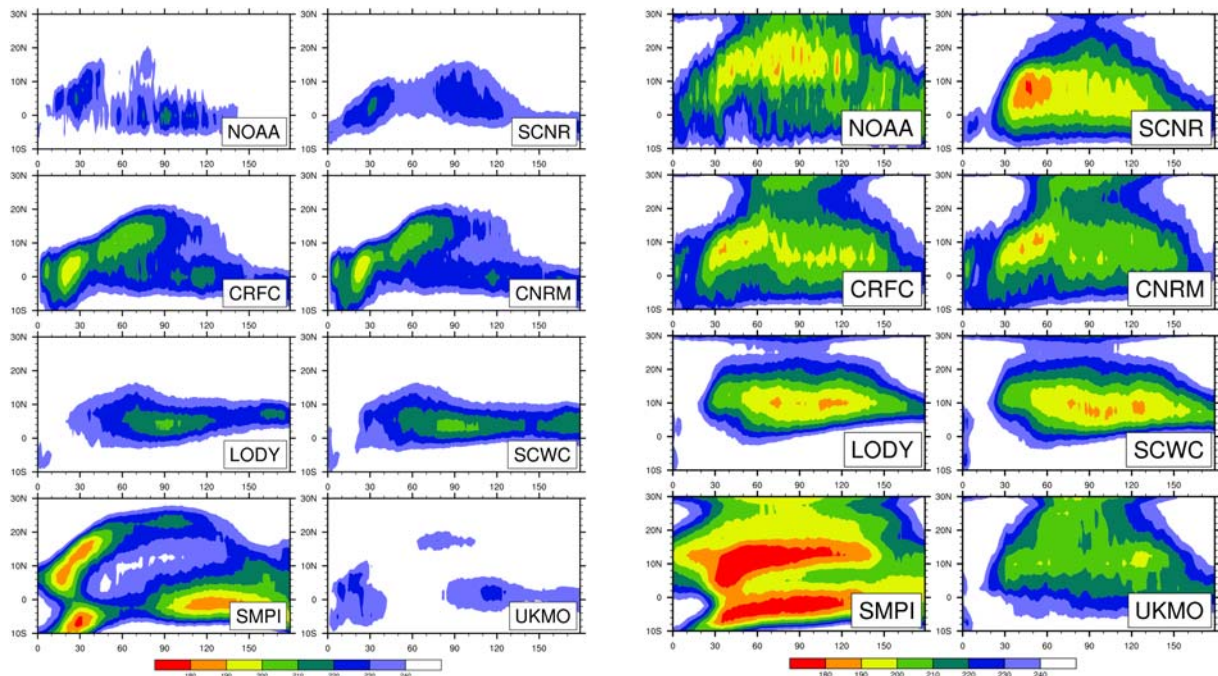


Figure 3: Time-latitude section of the climatological (average of 22 years for observations and 9 members and 22 years for models) daily evolution of OLR during the 180 days of hindcasts. The two columns on the left shows the average over the longitudes 50°-75°E (Arabian Sea) and the two right columns are the average between 75°-105°E (Bay of Bengal). Values are in W m^{-2} . X-axis is the hindcast days and Y-axis is the latitude.

3.2. Seasonal cycle

There are large seasonal variation over the Indian monsoon region between May and September. This also has an impact on the seasonal distribution of the location of the main convective intraseasonal events. The intraseasonal perturbations during summer are characterized by northward migration of the ITCZ from south of equator to about 25°N. In fact, first intraseasonal events in May and June of this northward transition are associated with respectively “bogus onset” (Flatau et al, 2001) in the south Bay of Bengal and onset of the Indian monsoon with strong amplitude in the Arabian Sea (Bellenger and Duvel, 2007). This gives significant differences in the seasonal variations between Arabian Sea and Bay of Bengal as also highlighted in Duvel and Vialard (2007). The skill of the models in simulating the seasonal cycle of monsoon is described here. Over Bay of Bengal (Fig. 3), a common problem for most the models is the lack of migration of ITCZ up to 25°N as in the observations. A distinct feature of the monsoon onset is the low OLR values over the Arabian Sea (mostly along the western coast of India), which has been reasonably well simulated in SCNR (Fig. 3) and UKMO, but it commences in mid-May for CRFC and CNRM. LODY and SCWC does not exhibit any significant seasonal variations, either over Bay of Bengal or Arabian Sea, with a narrow ITCZ that establishes around 10°N at the beginning of June and persists during the season. This indicates that the intraseasonal convective fluctuations will be restricted in this narrow region. On the other hand, SMPI has an exaggerated double ITCZ, with a faster northward migration over Arabian Sea in May and June compared to that over Bay of Bengal. UKMO, and CNRM/CRFC models give low OLR values north of 25°N with a quite realistic northward jump around day 60 of the hindcast (i.e. near 1st July). There is however a gap with larger OLR around 15°N (20°N) for UKMO (CNRM/CRFC) compared to observation.

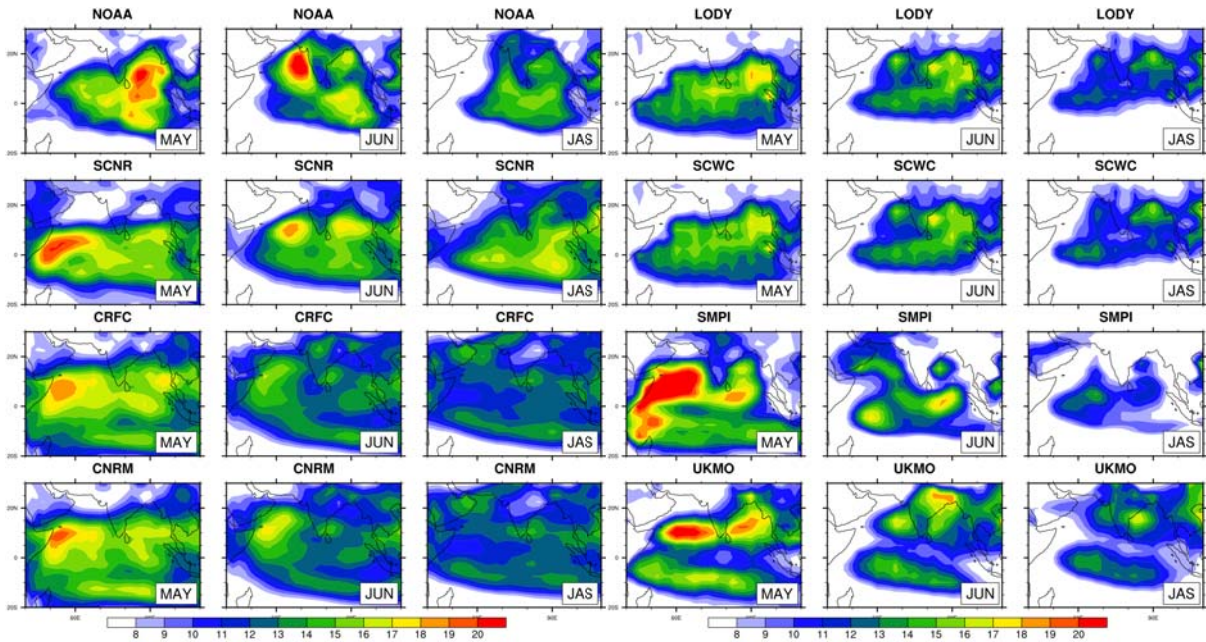


Figure 4: Climatological values of intraseasonal (20-90 days filtered) standard deviation of OLR for the months of May, June and JAS. 120 days of ERA40 OLR data has been prefixed to the hindcasts before filtering to avoid loss of information in the first two months of hindcasts (May and June), irrespective of the differences in initial conditions (Table 1). Values are in W m^{-2} .

3.3. Intraseasonal variability

Intraseasonal (20-90 days) variability is an important building block of the monsoon system, which exhibits strong spatial and temporal variability with the march of the seasons. Most of the studies that validated the intraseasonal variability in the GCMs (e.g. Waliser et al, 2003a) have considered the variability during the summer season as a whole and comparison of the average modes of the observations and models has been done. On a gross sense this may still be acceptable, owing to the large-scale behaviour of the ISOs. However, studies like Duvel and Vialard (2007) and Bellenger and Duvel (2007) indicate strong seasonality in the amplitude, organization and reproducibility of the summer ISOs, related to the seasonally varying air-sea processes and the seasonal variations of the oceanic mixed layer. The climatological ISV in these coupled hindcasts are evaluated here for different phase of the monsoon season. The ISV is extracted by applying a 20-90 days Lanczos (Duchon, 1979) filter with 90 weights, with 120 days of ERA40 data prefixed to each hindcasts. This filtering procedure may introduce some biases in May and June (see section 6) due to the contrast between ERA40 OLR and the OLR of the different models. Larger errors are expected for models with initial conditions other than ERA40 (SCNR and SMPI). Therefore, the ISV of SCNR and SMPI for May and June may be treated with caution.

The features of the seasonal march of the monsoon and of the ISV are detailed in Duvel and Vialard (2007). The most striking features are the strong convective fluctuations (analogous to the large OLR amplitude) over the Bay of Bengal and the eastern Indian Ocean in May associated with the commencement of the northward propagation of the ITCZ and the low level wind flow across the southern parts of India resulting in rainfall (often referred to as bogus onset; Fig. 4).

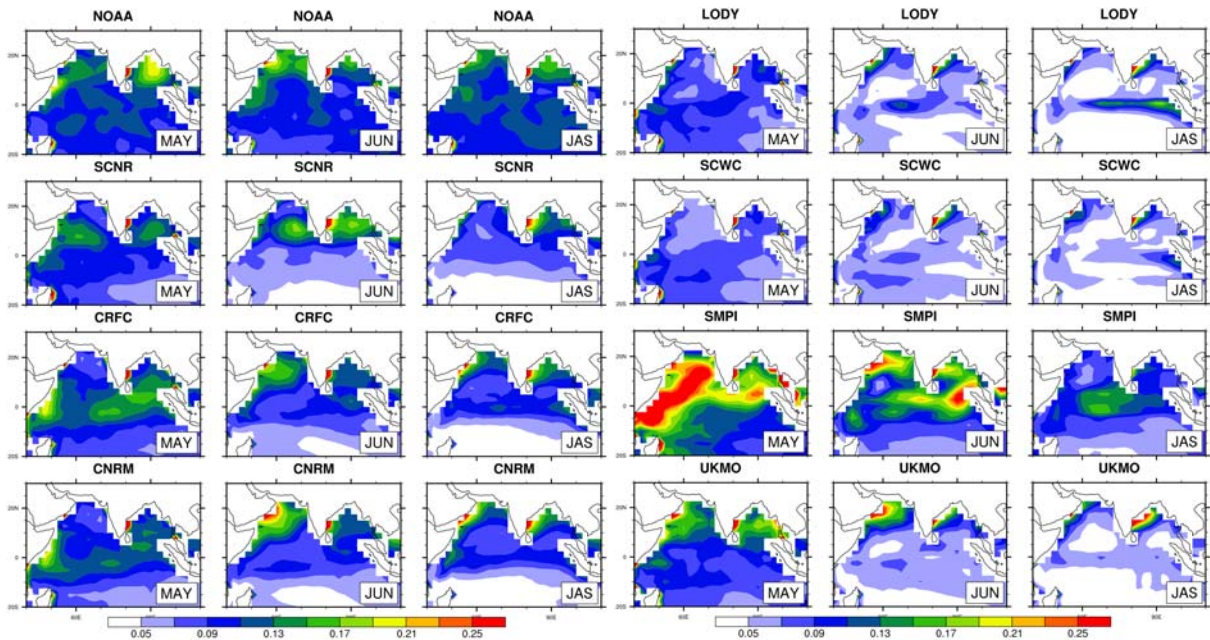


Figure 5: Same as Fig. 4, but for the SST (units are in K).

In May, the shallow mixed layer depth (MLD; from de Boyer et al. 2004 climatology; Fig. 6) over the northern Bay of Bengal is compatible with a rather strong response of the ocean temperature to the convective perturbations further south (Fig. 5). Note that the deepen MLD south of Bay of Bengal is consistent with the development of the bogus onset here (the climatological MLD is smaller in April). The perturbations of the SST on the west side of the Bay of Bengal and the Arabian Sea may be attributed to the fluctuation of the upwelling linked to fluctuation of the monsoon low-level jet. With the progression of the season, the largest convective intraseasonal event is observed in June over the Arabian Sea (Fig. 4). Two secondary maxima are found, one over the east equatorial Indian Ocean and another over the northern Bay of Bengal. The strengthening of surface winds at the time of the monsoon onset causes a progressive deepening of the mixed layer in both the Arabian Sea and Bay of Bengal (Fig. 6). As a result, the largest SST variability is more confined to upwelling regions and to the northern Bay of Bengal and Arabian Sea where the MLD remains shallow. Note that the ISV, that is clearly maximum over ocean region, is weaker between July and September (JAS). This shows that the larger ISV is associated to monsoon and bogus monsoon onsets. The decrease of the ISV during JAS may be attributed in part to the deepening of the mixed layer (see Bellenger and Duvel, 2007 for further discussion).

Some of these climatological features of the ISV and their seasonal variations in the models are evaluated here against those observed. The monthly averaged MLD of only two models (CRFC and SCWC) are used in the present analysis as preliminary tests. The SST in the models also is the temperature of the first model layer and hence the effects of certain observed processes such as the warm layer formation may explain part of the model bias.

LODY and SCWC produce primary variability of convection in May in the Bay of Bengal similar to the observed (Fig. 4) but with reduced magnitude. The shift of the ISV centre to the eastern Arabian Sea in June does not dominate in these simulations and the ISV of the SST is weak. The MLD of SCWC shows (Fig. 6) that the model has very deep mixed layer in May and it deepens further with the march of the season. This deep mixed layer might be an important cause of the reduced SST variability in this model. CRFC and

CNRM have significant biases in simulating the convection variability in May (maxima of convection variability is simulated in the western Arabian Sea, instead of Bay of Bengal, Fig. 4) and so does the locations of SST variability (Fig. 5). Mixed layer of CRFC in May is shallow compared to observations in the western Arabian Sea, parts of Bay of Bengal and the central Indian Ocean (Fig. 6). This could partially explain the large SST variability in this model in these regions.

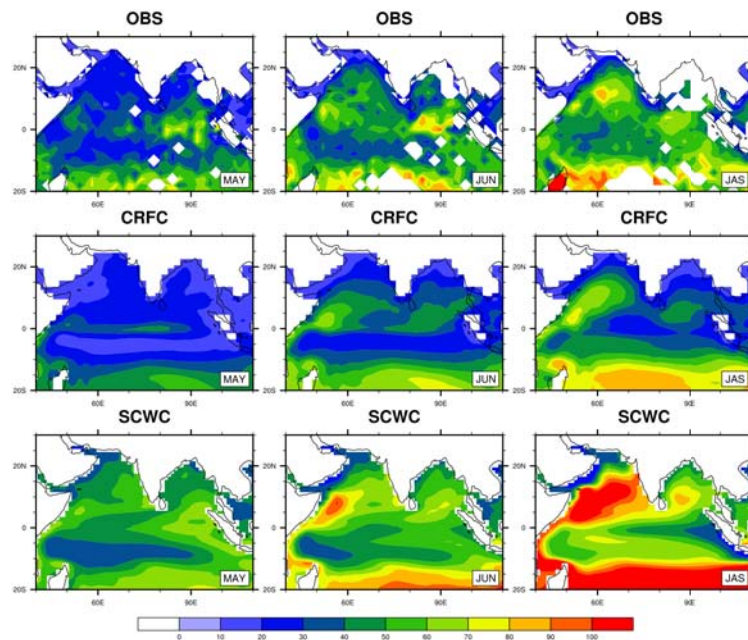


Figure 6: Climatological values of mixed layer depths (m) for the months of May, June and JAS from de Boyer et al. (2004) climatology (top panels) and from CRFC (middle panels) and SCWC (bottom panels).

In terms of the OLR variability in May, SCNR and SMPI may be interpreted with caution. Since these two models have different atmospheric initial conditions than ERA40 (Table 1), the use of filtering with prefixed ERA40 data could have introduced certain amount of artifacts other than the intrinsic biases of these models as shown in Fig. 1-5. The large intrinsic model biases of SMPI along with the filtering might have amplified this biases compared to that of SCNR. However, the effect of filtering is present in May and June and a direct model to observation comparison may be meaningful only for JAS for these two models. Despite this possible source of error, SCNR has better resemblance than any of the models to the observations in JAS. However, the maxima of OLR are located to the south compared to the observations. An intriguing feature is the similarity of the patterns of OLR and SST variability in SMPI during JAS. Though this model does not simulate most of the observed features, this strong correspondence in the OLR and SST variability, points to a rather strongly reacting ocean, possibly with a shallow mixed layer (i.e. possibly the first layer of the ocean model) that integrates the surface heat fluxes and the other processes such as mixing of subsurface waters. Most models have strong OLR variability over the western Indian Ocean, close to the Somalia coast in May. This being a strong convergence region, the unrealistic OLR variability may be related to the closure in the convection parameterization in the models. This may be also related to the transition from the ERA-40 to the model OLR close to the start of the hindcast (see above for shortcomings in the current procedure).

Despite some of the important biases of the simulations presented above, the seasonality in the character of the ISV in OLR and SST is simulated to certain level of accuracy by all models. All models exhibit large

ISV in May and June and proportionally reduced variability during the rest of the season (JAS, Figs. 4 and 5). With the MLD of two models (CRFC and SCWC, Fig. 6) it may be verified that a progressive (wind induced) deepening of the mixed layer during the JAS period is represented by both the models, despite the intrinsic model biases. The features discussed above may be summarized in Fig. 7, which shows values of the area averaged OLR ISO standard deviation (over the entire domain of Fig. 4) for each model for May, June and JAS season. This can also be considered as a measure of the biases of the seasonal cycle of each model. A proportional weakening of ISO activity from May to June is exhibited by most models, i.e. models with stronger ISV in May compared to the observations tend to have stronger variability in June also. This relationship may be fundamental to the seasonal cycle in the atmospheric models. This conclusion is derived from the fact that the amplitude of ISV in May, June and JAS is almost identical for the models with the same AGCM (Table 1). We have here two pairs of AGCMs coupled to different OGCMs (CNRM-CRFC and LODY-SCWC), with the former pair having a consistently stronger ISO activity compared to observations throughout the season, while the latter is weaker in magnitude.

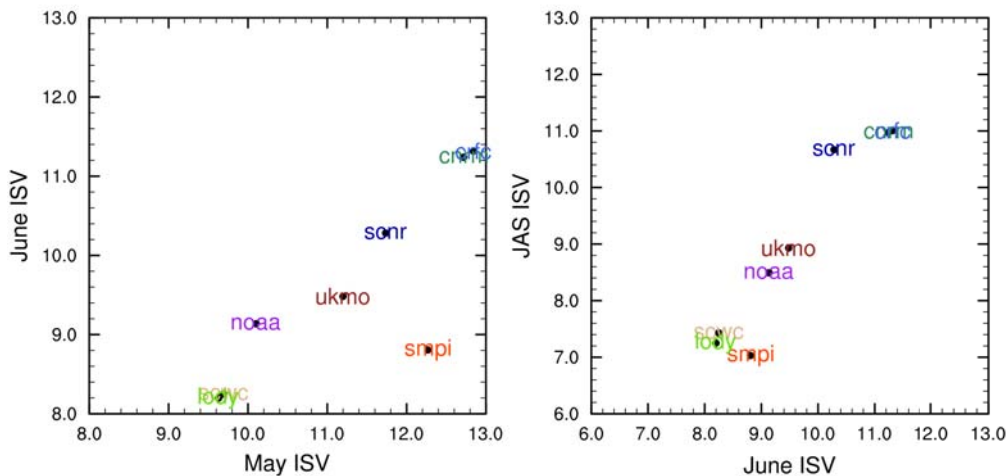


Figure 7: Scatter plot of area averaged intraseasonal variability (represented as standard deviation in W m^{-2}) over the region $40^{\circ}\text{-}110^{\circ}\text{E}$, $20^{\circ}\text{S}\text{-}30^{\circ}\text{N}$ between May and June (left panel) and between June and JAS (right panel) for each model and the NOAA OLR.

It has been shown using coupled and uncoupled simulations that air-sea coupling may modify the structure of the intraseasonal variability (Kemball-Cook and Wang, 2001; Fu et al, 2003). However, even when coupled with very different OGCMs (OPA version 8.1 and HOPE, Table 1), the basic properties of the IFS model remain almost similar. Air-sea coupling is therefore important, but the basic characteristics of the coupled model could arise from the AGCMs. In addition, the ocean models considered here might have certain limitations in simulating realistic SST variability for the following reasons. As previously mentioned, the formation of warm layer over the oceans in clear and calm conditions play a role in the air sea interactions at intraseasonal time scales and are capable of triggering large scale organized convective perturbation that later evolve at the intraseasonal time scale. The considered OGCMs have poor resolution at the top of the ocean (say 10 m at the best) and have thus very limited potentials for simulating these kind of diurnal variations of SST. Due to the same reason (poor vertical resolution), there could be uncertainties in the determination of the oceanic mixed layer and its variability on the intraseasonal time scales. Another factor may be the lack of representation of fresh water from the rivers in to the north Bay of Bengal in the models, which, can actually have significant impacts on the air sea interactions over the region (Sengupta and Ravichandran, 2001).

4. Evaluation of the organized ISO in the hindcasts

A more quantitative assessment of the character of the ISV represented in the models is performed in this section. In order to illustrate the space-time variability associated with each model's ISO, we employ the LMA (Goulet Duvel, 2000; Duvel et al, 2004; Duvel and Vialard, 2007). In order to avoid the loss of information at the beginning of the hindcasts (1 May and 1 November) while performing CEOFs on the 90-days window, 120 days of ERA40 OLR are prefixed to the hindcasts. While LMA provides a wealth of information on the ISO characteristics mentioned above, we concentrate on the seasonality in the organization of the modes, propagation characteristics, and the air-sea interactions associated with large-scale organized perturbations of the convection. In order to demonstrate the seasonality in the character of ISOs as seen in the ISV maps in Fig. 4, the average modes of OLR for May, June and July are constructed (Fig. 8). Similar behavior of models with the same AGCMs (as in the previous figures) has been observed here also. Therefore, figures for CNRM and LODY are not shown here, since the characteristics are almost identical to that of CRFC and SCWC respectively.

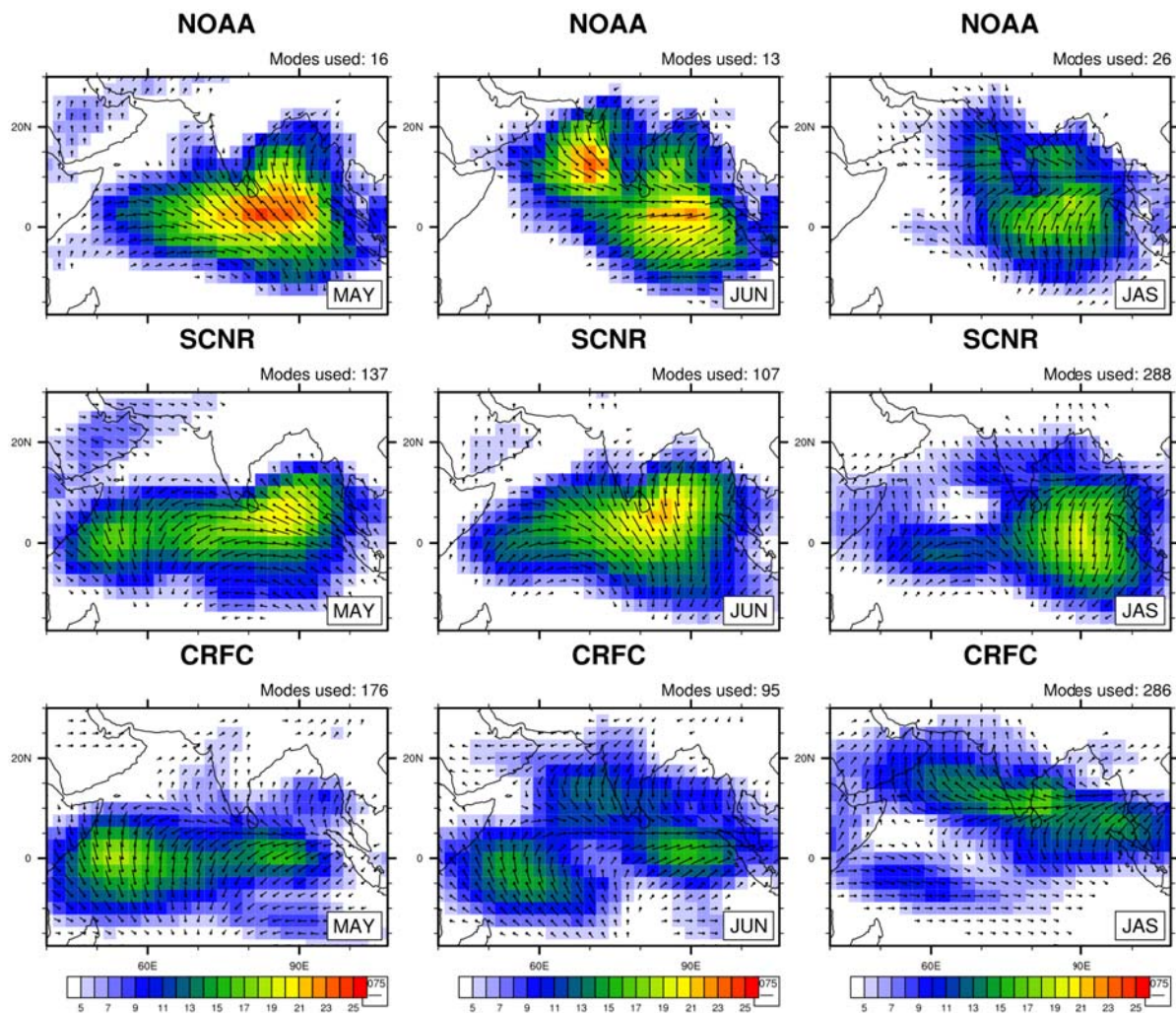


Figure 8: The average of local modes of OLR for May, June and JAS. The number of local modes used to construct each pattern is indicated on the top right of each panel. The segment length is proportional to the standard deviation and the angle of the segments represents the relative phase. The angle increases clockwise with time (e.g. northward propagation for a segment rotating clockwise towards the north). Shaded represent the standard deviation of these patterns in W m^{-2} .

Strong seasonal variations in the organization and location of modes are exhibited in all models consistently with Fig. 4. But, no model simulates the dramatic shift of intraseasonal activity from May to June associated with the monsoon onset. There is an extension of ISO amplitude towards the equatorial western Indian Ocean in almost all models during all the summer months. If one considers only the propagations of intraseasonal convection perturbations, SCNR and CRFC (and CNRM, but not shown) are better than the rest of the models due to their large-scale organization and northeastward propagation from the western Indian Ocean. However, SCNR has a dominant eastward propagation that might explain why the convection does not reach the northern Bay of Bengal in this model, despite having a better spatial organization of the amplitude of the convective perturbation.

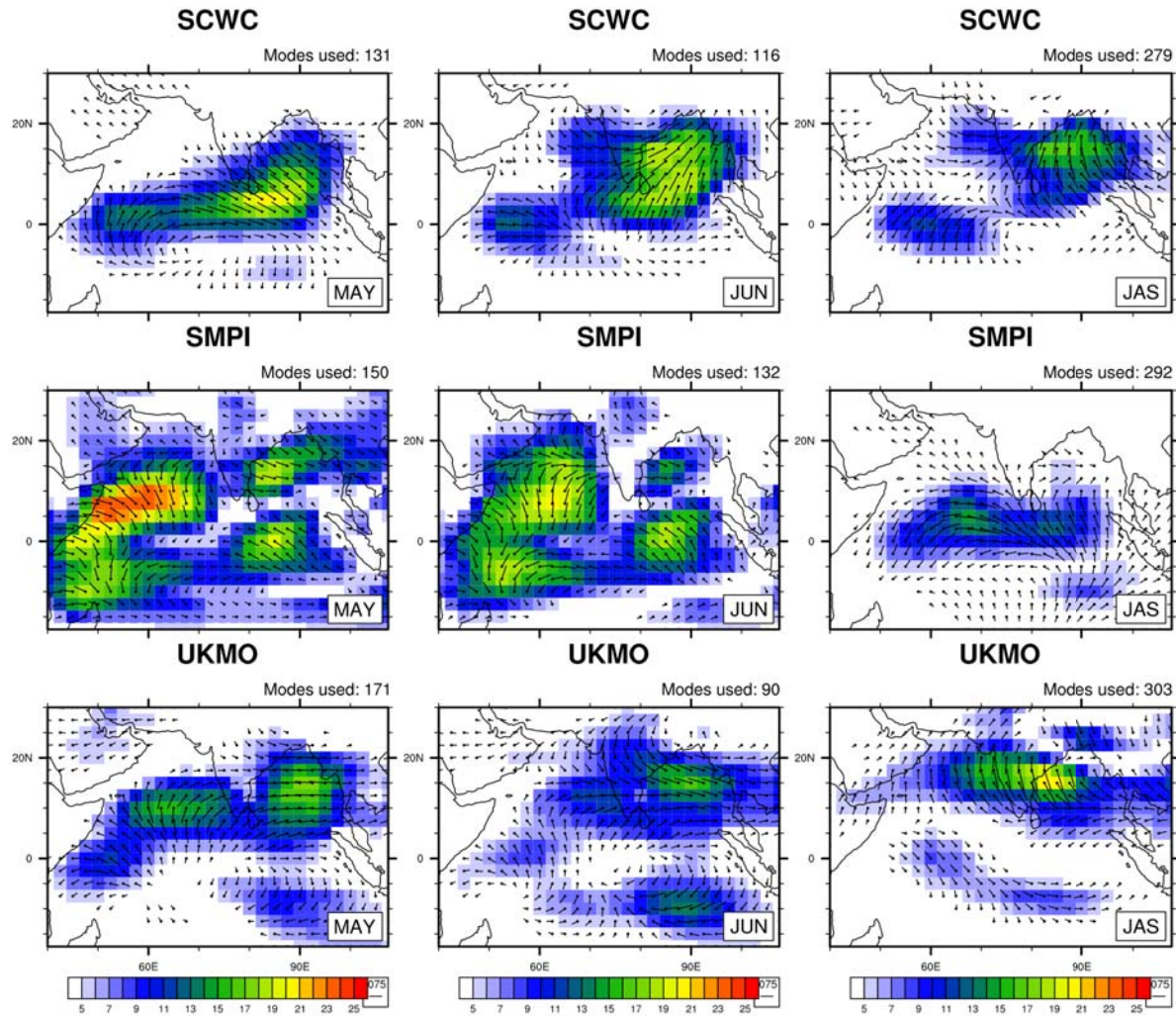


Figure 8: Continued.

There appears to be a relationship between the seasonal cycle of OLR and the organization and propagation of convection perturbations as shown by SCWC (and LODY) and UKMO. These models have strong biases in the seasonal variations of OLR (Figs. 3 and 4). The JAS perturbations over the Bay of Bengal in SCWC has properties of a standing mode, with a weak westward propagation over India to the Arabian Sea, whereas in UKMO there is clear westward movement of convection from the Bay of Bengal, typical of a Rossby wave propagation. This linkage between the seasonal cycle of convection and the intraseasonal properties of convective perturbations may be related to the physical parameterization in the models. For example, a

model that fails to organize convection over a large region could produce small cloud clusters, which do not exhibit any organized behaviour and that might not be able to drive large-scale dynamical response and the corresponding large-scale air-sea processes. In such a situation, the ocean feedback to the atmosphere in further organizing the convection will be weak, resulting in poor representation of the ISO properties.

4.1. Winter ISV

Even though the major focus of this study is on the summer variability over the Indian Ocean domain, the analysis has been also extended to the winter hindcasts (starting from 1 November). Often referred to as MJO, these convective propagations, which are stronger (i.e. organized at a larger Indo-Pacific scale) in winter than in summer, initiate over the tropical Indian Ocean and propagate eastward. To facilitate comparison of the properties of summer ISO, LMA for the winter hindcasts are also performed in the same way as described in Section 2, but over a domain that has larger zonal extension (40° - 160° E) to include the large-scale structure. Since there is less seasonal variability of the modes in winter compared to summer over this region, only the average modes for the whole winter (November to March) are shown (Fig. 9). Because of the very similar behaviour of the pairs CRFC/CNRM and SCWC/LODY, only the results for CRFC and SCWC are shown.

SCNR shows a quite realistic eastward propagation despite too strong amplitude over the maritime continents. While the eastward propagation is well reproduced, the maximum amplitude in CRFC is shifted to the central Indian Ocean. This shifts the wind and SST responses to the western Indian Ocean (not shown) in agreement with the observed Gill type dynamical response (Gill, 1980). As for the summer case, SCWC, SMPI and UKMO have poor simulation of the winter ISO modes with almost no variability along the equator and with westward Rossby-type wave propagation in SMPI and UKMO.

4.2. Air-sea interactions

Using the multivariate LMA approach, it is also possible to compute the SST and wind patterns associated to the OLR local modes. These patterns thus represent SST and surface wind perturbations associated to the large scale organized convective perturbations. It is also possible to obtain the patterns for the average response of SST and surface winds to large scale organized OLR intraseasonal perturbations.

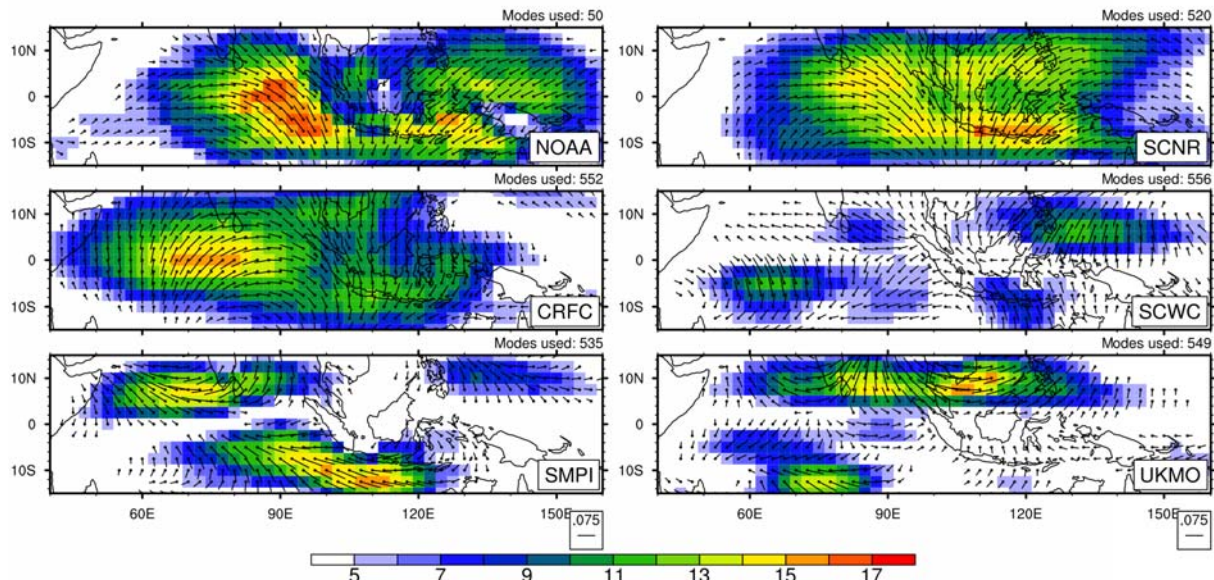


Figure 9: Same as Figure 8, but the average modes for November to March season from the hindcasts starting on 1 November. Larger spatial domain has been used in order to incorporate the large scale zonal structure of the winter ISOs. Shaded indicate the standard deviation of the average mode and the segments represent the phases of the mode. Progressive clockwise rotation of neighbouring grid points to the east indicate an eastward propagating mode.

During the summer season, the ISV of convection is maximal over the northeastern Bay of Bengal and around the Indian subcontinent (with relative minimum over the subcontinent), suggesting the importance of air-sea coupling on the intraseasonal time scales. The ISV of SST is strong in the northern Bay of Bengal and Arabian coast and the surface wind perturbations also have maxima over these two regions (Duvel and Vialard, 2007). The average phase relationships between the OLR, SST and surface winds are shown here (Fig. 10) that can explain some of the processes of air-sea interactions in this region. If the convection and winds are in phase (i.e. maximum wind for maximum convection), one expects a $\frac{1}{4}$ period lag of the SST with respect to OLR if surface fluxes were the dominant process that drives SST fluctuations. However, in reality, this quadrature relationship holds good over some regions only for which the atmospheric heat fluxes appear to be the dominant factor for SST variability. For other regions, there could be influence of other processes such as the warm layer formation or upwelling in determining the SST. Only SCNR (despite some of the possible sources of biases as mentioned) has some fidelity in simulating these features, while most models indicate a nearly perfect quadrature relationship between SST and OLR over Bay of Bengal and eastern Indian Ocean (CRFC is shown as an example for the other model with similar behavior).

The phase relationship between winds and SST due to other processes is however more variable in regards to this $\frac{1}{4}$ lag of period related to the simple integration of surface fluxes by a mixed layer of nearly constant depth. For example, in the presence of a warm layer, prior to the convective perturbation, the daily mean SST will tend to be maximal for the minimum wind and will sharply decrease towards the average mixed layer temperature as soon as the winds rise above certain threshold. Even if the mixed layer temperature then evolves under the influence of surface flux forcing, the phase relationship between SST and winds will be modified by this warm layer formation and destruction with the SST becoming more in phase opposition with the surface winds. A similar behaviour is expected for a rapid deepening of the mixed layer because of wind burst that gives a fast cooling related to the mixing with deeper and colder waters. This nearly $1/8$

phase difference between SST and winds are reproduced to some extend only in SCNR with the covariability nearly on the same regions. An example of the typical behavior of all the other models is shown here as CRFC. Even with a rather reasonable simulation of the mixed layer, it produces too systematic relationship between the three parameters over these key regions.

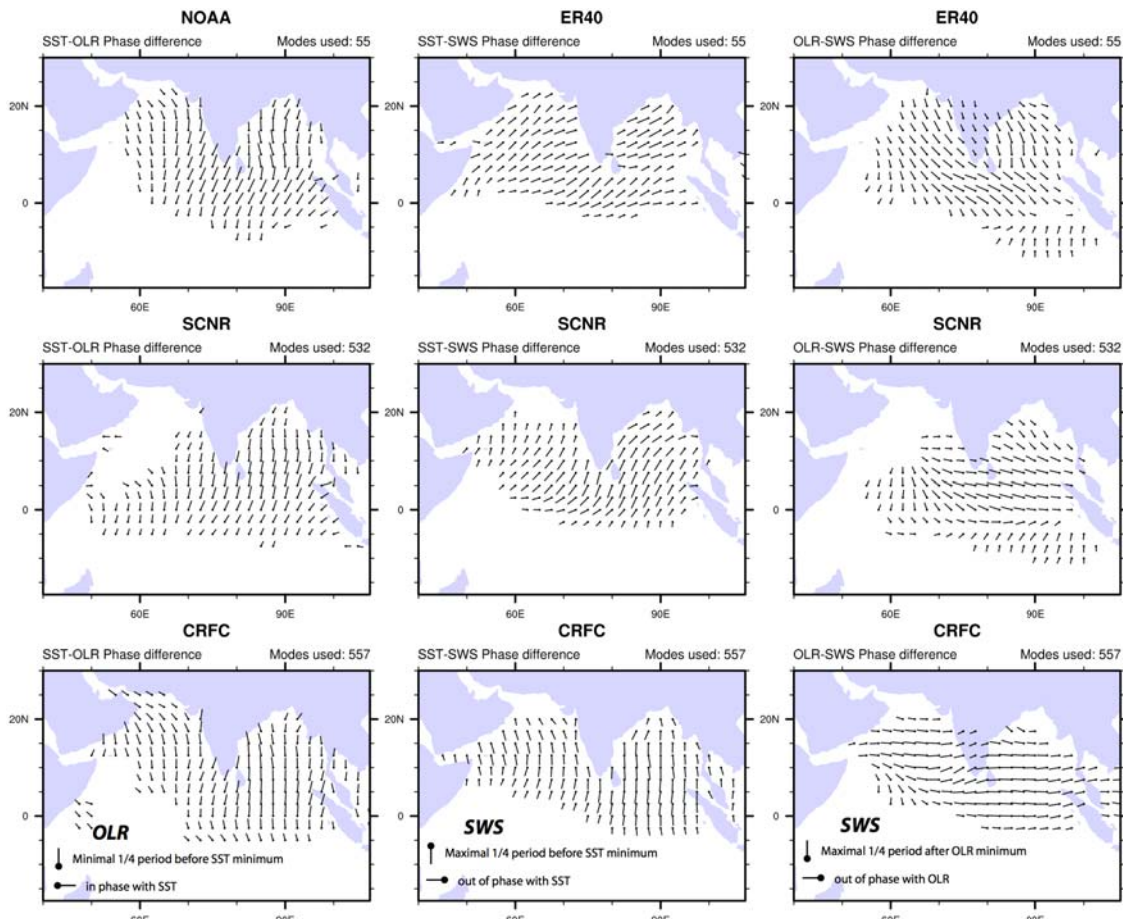


Figure 10: Phase difference between the SST perturbation and the OLR (left), between SST perturbations and the surface wind speed (middle) and between OLR and surface wind speed (right) for the summer season. For the left figures a northward (eastward) pointer means that the OLR is minimal $\frac{1}{4}$ period before (simultaneous with) the SST minimum. For middle panels, a southward (westward) pointer means that the surface wind speed is maximal $\frac{1}{4}$ of the period before (simultaneous with) the minimum SST. For right panels, a southward (westward) pointer means that the surface wind speed is maximal $\frac{1}{4}$ of the period after (simultaneous with) the minimum. Segment length is proportional to the product of normalized standard deviations of both considered parameters.

For boreal winter (Fig. 11), the maximum perturbations of these three parameters are maximal south of the equator, off the northwest coast of Australia for a region of relatively thin mixed layer. Over the Indian Ocean the delay between the SST and OLR is close to $1/8$ of the period and so is the phase between SST and winds. The surface wind is maximal shortly after the maximum convection, giving a nearly in phase modulation of the solar and turbulent fluxes that will reinforce the SST perturbations. The only model that reasonably simulates these complex features is SCNR. Most of the models have very systematic relationships between the parameters (CRFC shown here as an example).

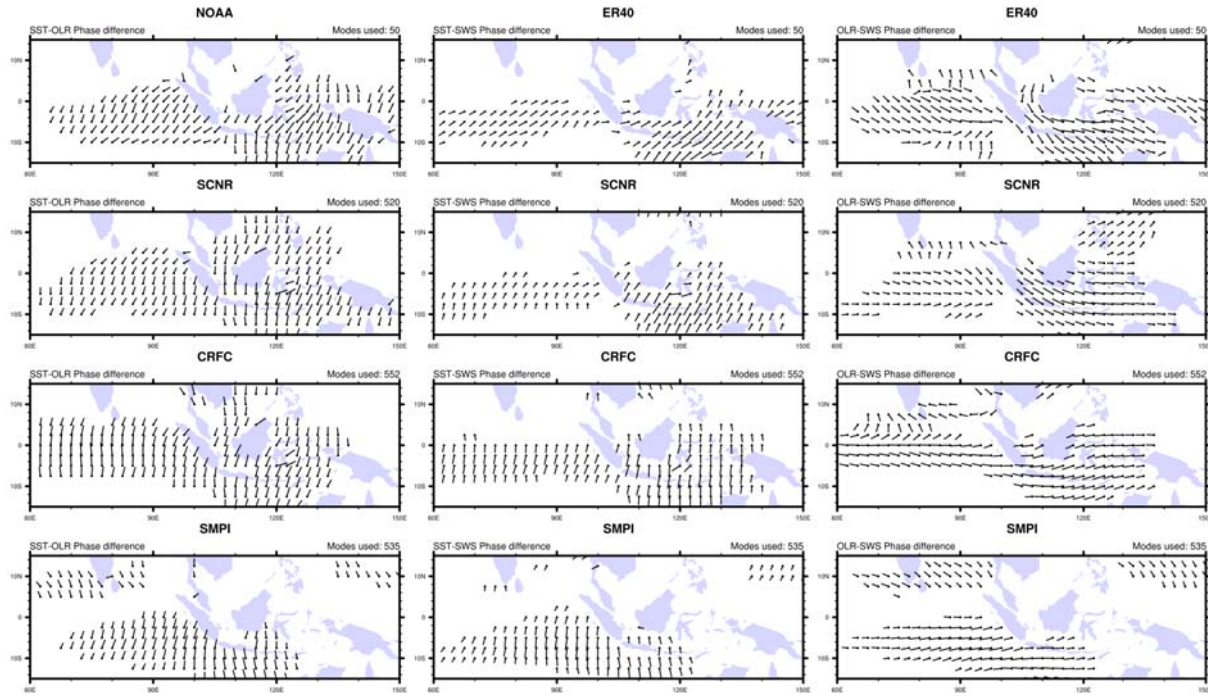


Figure 11: Same as Figure 10, but for the winter hindcasts.

4.3. Period, degree of organization and distance of local modes from the average pattern

An important use of LMA is to diagnose some of the biases of the models in terms of the organization of convection, and the reproducibility of the modes. A mode that has a longer period tends to organize in large scale due to its slow evolution. Even for a simple slab ocean type of SST response, atmospheric forcing acting for a sufficiently long time can integrate the surface fluxes and result in significant SST perturbations. The large-scale organization of the convective perturbation is thus crucial for organizing SST perturbations. This organization is also crucial to correctly reproduce the dynamical response associated to the tropospheric heating.

Since the ISV is not purely harmonic, the period of an ISV event is not perfectly defined. The method adopted here to compute the period for each local mode is the same as the one explained in Goulet and Duvel (2000), which computes an average time scale from a sum of phase differences between two time steps weighted by their average amplitude. Since LMA extracts a pattern for each event (i.e., each local mode), it is possible to measure the resemblance between an average pattern and the patterns of each ISV event, and thus verify how representative the average pattern is of the various events considered.

Another parameter of interest that can be extracted using LMA is the level of organization of individual local modes. The percentage of variance explained by each of the local modes explains the degree of organization of the modes. This section describes the inter-model differences in these parameters and how they differ between summer and winter. Since SCNR and SMPI have different atmospheric initial conditions (Table 1) compared to the rest of the models, and due to the application of a filter with ERA40 data prefixed to the hindcasts, there is possibility of some uncertainties in the definition of the modes and their properties for May and June.

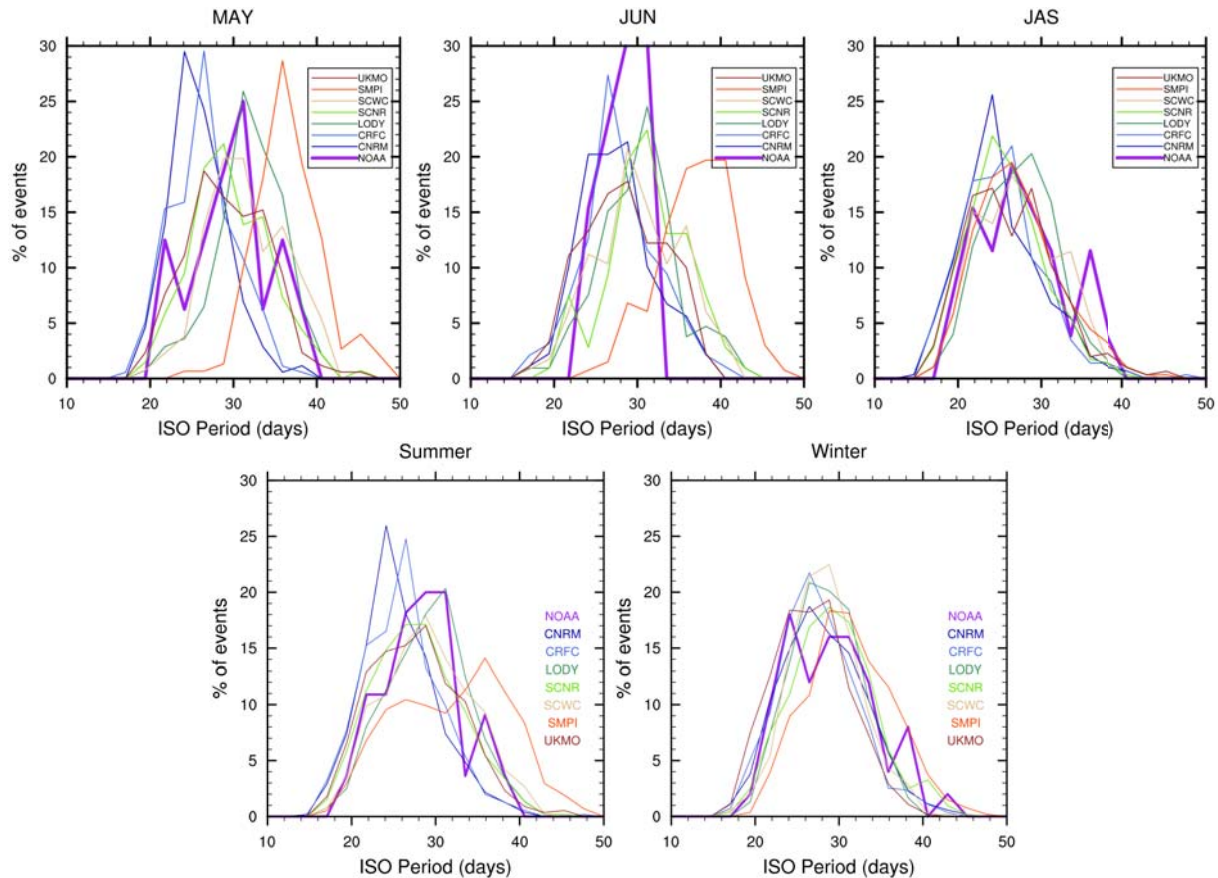


Figure 12: Histograms of the periods of local modes centered in May, June and JAS months (top 3 panels). The two bottom panels show the histograms of the periods of all local modes in the summer (May-September) taken together, and the periods of all local modes in winter (November to March).

The histogram of the periods of the local modes from summer and winter hindcasts are given in Fig. 12. There is strong seasonality in the period of the observed modes with shorter period in boreal summer and a well-defined preference for period around 30 days in June. In May and June, there is a large spectrum of behaviour for the different models. This can be mostly related to the disparity between ERA-40 OLR and model OLR in the same 90-day time section giving spurious Local Modes, especially for SMPI, as discussed above. For JAS, the period distribution for the different models is relatively good despite a tendency for shorter period for some models.

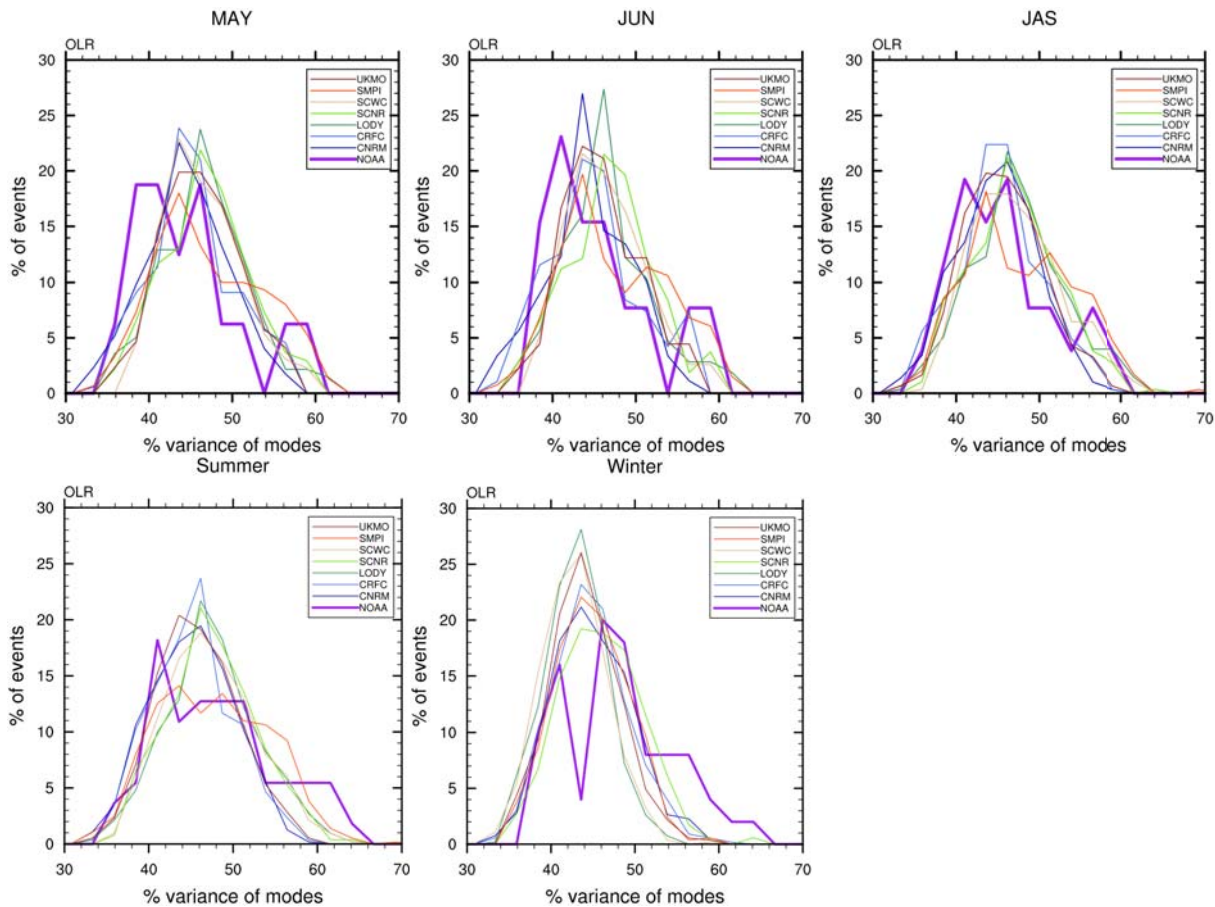


Figure 13: Histograms similar to that of Figure.12, but for the percentage of variance explained by each local mode. A large value of percentage of variance indicates modes with large scale organization.

There are a larger proportion of organized (percentage of variance larger than 50) and unorganized (percentage of variance lower than 40) modes in the observations than in the models (Fig. 13). This indicates a larger variability of the degree of organization of the convection with well organized modes that never appear in the simulations. The potential errors due to the different initial conditions of SMPI and SCNR appear as more reproducible modes in May and June (Fig. 14). This should not be mistaken as closely repeated modes in May and June as in the observations (especially in June). The effect of the mixing with ERA-40 OLR in 90-day time section would no longer be present in the JAS modes. SCNR produces slightly better reproducible modes than the other models in JAS, but with significantly less reproducibility compared to the observed modes (Fig. 14). When taken together all the summer and winter modes, the models clearly appear to be unable to generate reproducible modes. This is a fundamental result showing that the physics of the different models is currently unable to organize the convective activity in a consistent and reproducible manner. There is clearly a missing process in these coupled model, may be related to the air-sea interaction.

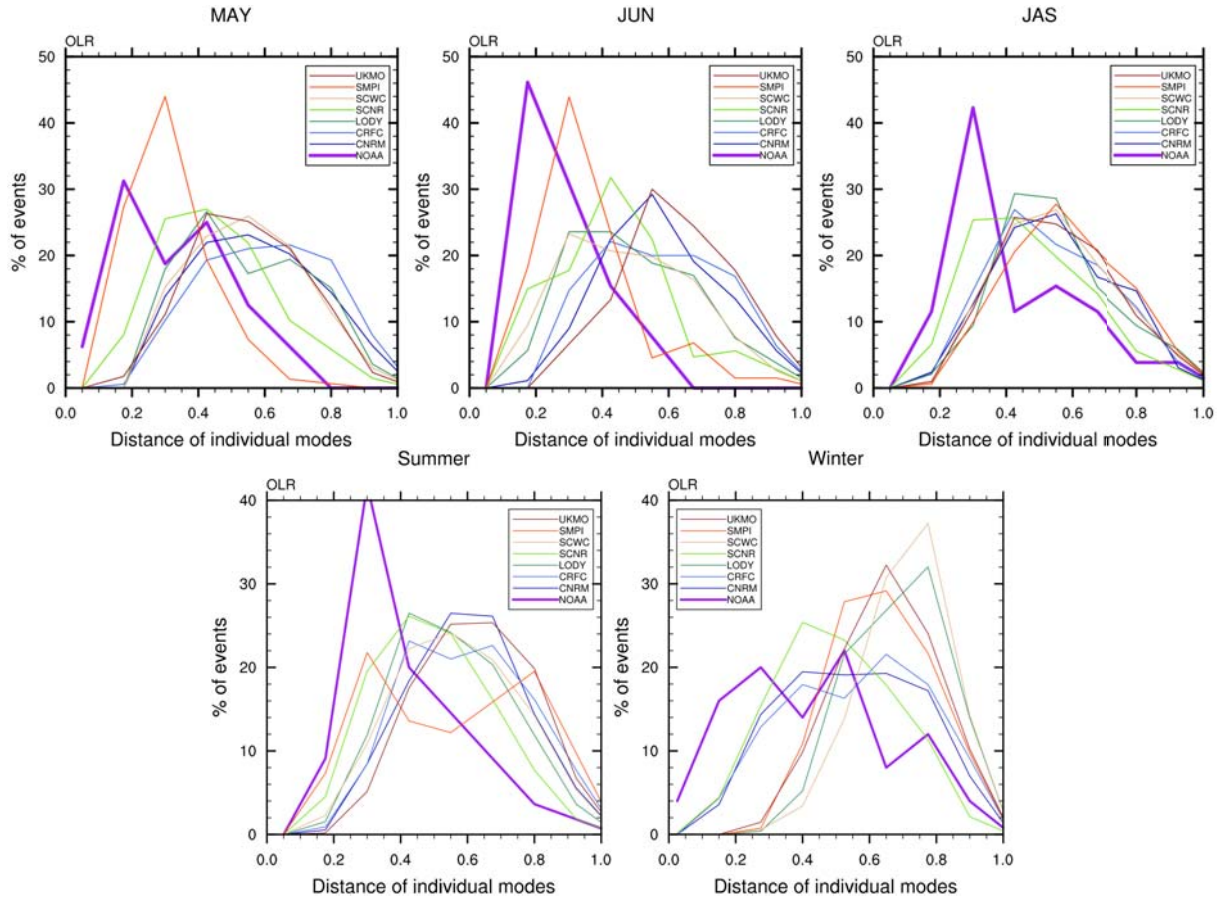


Figure 14: Histograms of the distance of individual local modes to the average patterns for the observations and models for May, June and JAS (top panels). Histograms of the distances of all the summer modes and winter modes taken together is also given for comparison. A distance value zero indicates that the local mode is perfectly represented by the average pattern and 1 means they are orthogonal.

5. Evaluation of the extended range (20-50 day) predictability

Although improved simulations of the tropical ISV may have potential to improve the long-range forecasts, the practical realization of this effect is hampered by the biases discussed above. The exact mechanisms of this variability are not yet clearly understood. Additional problems arise from the large observational errors that are contained in the tropical analysis. However, the intermittent, large scale organized and quasi-periodic nature of the ISV should impart certain predictability proportional to its own lifetime (Van den Dool and Saha 1990). The recurrent behavior of ISV could be utilized for extended range forecasts of about a month. Some empirical models have already indicated useful skill out to about 15-25 days lead time (Waliser et al. 1999, Lo and Hendon 2000, Goswami and Xavier 2003, Webster and Hoyos, 2004). Most studies have supported the notion that air-sea coupling could improve the simulation of tropical ISV (Flatau et al. 1997, Wang and Xie 1998, Waliser et al 1999b, Kemball-Cook et al. 2002, Fu et al. 2003). Fu et al 2007 showed using ECHAM4 coupled to a tropical upper ocean model with intermediate complexity, that coupled models have improved predictability (about 24 days) compared to its uncoupled counterpart (17 days).

Most of the studies mentioned above compute the potential limits of predictability but the actual predictability (model-observations comparison) has not been evaluated for different models. Here we

evaluate the potential and actual limits of predictability in the DEMETER hindcasts as follows. The hindcasts time series are averaged on pentad (5-day) in order to eliminate some of the high frequency synoptic scale variability. For each of the summer and winter hindcasts, spatial correlations over sufficiently large domains (60° - 120° E, 10° S- 30° N for summer hindcasts and 70° - 140° E, 10° S- 10° N for winter hindcasts) are computed at each hindcast pentads between each of the 9 members taken two at a time. The average spatial correlations of all these (36) combinations among the 9 members averaged over the 22 hindcast years is denoted as the potential predictability of a particular model at different pentads. This in other terms is a measure of the internal variability of the model and if a model has large member-to-member consistency, the member-to-member spatial correlations remain high. The lead-time up to which these correlations remain significant could be interpreted as the potential limit of useful predictions by the model, assuming a perfect model scenario. However in reality no model performs close to the observations as evident from the evaluation of the model simulations. Therefore, there is an actual predictability attained by each model when compared to observations. This actual predictability is also computed similarly, but spatial correlations of each member are calculated with the corresponding observed values.

These spatial correlations for summer and winter are given in Fig. 15. The potentials for prediction of the ISV in summer appears far more superior to the winter with all models (except SMPI) maintaining correlation values above 0.6 even up to 10 pentads in summer. While in winter the potential predictability of all models (except SMPI) drops below 0.4 between 2 and 5 pentads. For SMPI, the inter-member consistency drops in the first pentad itself due to the rather large differences between the atmospheric conditions the 1st may given by the particular initialization procedure. All the model hindcasts evolve a few pentads under the influence of the initial conditions. The inter-member variability then converges toward a value corresponding to the climatological stochastic variability of the model. This behavior is seen in the winter hindcasts also but with a proportional reduction in the correlations.

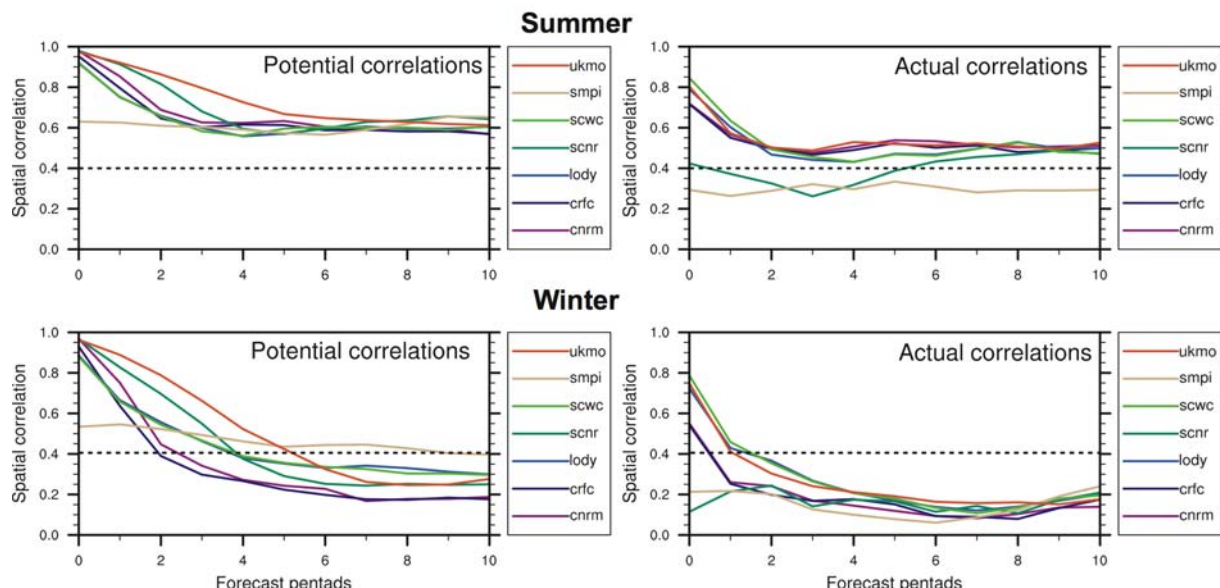


Figure 15: Potential and actual spatial correlations of the summer and winter hindcasts. Potential correlation is computed as follows: The spatial correlations (over 384 and 224 grid points in summer and winter respectively) among the 9 members taken 2 at a time (36 values per pentad per year) are first computed. The average of these 36 values for all the 22 hindcast years gives the potential correlation for a pentad. Actual correlation for a pentad is computed as the average spatial correlations between each member and the observations (9 values per pentad per year) for all the 22 hindcast years.

Consistent with the potentials for summer and winter, the actual observed correlations are also significantly different. For the summer hindcasts, most models show significant correlations with observations for the first pentad but drop rapidly from initial pentad to the second pentad, they improve slightly at pentads 5 and remain at a level of 0.5 till 10 pentads. This feature of most models is rather important since most models have the ability to predict the large-scale organization of convection associated to the monsoon onset at the beginning of June (nearly the 6th pentad). Due to the different initializations, SCNR and SMPI start with low correlations, but SCNR starts to develop better agreement with the observations at 5 pentads and remains in the group of the other more skillful models. The skill of SMPI (potential and actual) is far lower than the rest of the models in summer. The IFS models (LODY and SCWC) have better skills in the medium range (up to 2 pentads) while CNRM, CRFC and UKMO show better skills in the extended range (3-8 pentads). As one would expect from the potential skills in winter, the actual correlations are not better beyond the limit of medium range forecasts. A conclusion derived from this analysis is that the models with better summer predictability are also the models with better winter predictability. The improved predictability in summer may be attributed to the part of the seasonality that each model is able to represent, with models having better simulations of the seasonal cycle (Figs. 3 and 4) tend to have better predictability, especially for CRFC, CNRM and UKMO, that show well defined seasonal cycle that is consistent among different members.

It has been shown in several studies (Waliser et al 2003, Goswami and Xavier 2003, Fu et al 2007) that the predictability of tropical ISV depends on the initial phase of the convection from which the forecasts are started. It is equally important to understand the impact of the large-scale organized perturbation of the convection around the initial date of the hindcast in the medium to extended predictability of the ISV. Using LMA this could be examined in detail. The future work will focus on this aspect.

6. Evaluation of the seasonal predictability

6.1. Predictability of the intraseasonal activity (Boreal Summer)

After 10 to 20 days, the predictability of intraseasonal events is expected to be only statistical. There is indeed no possibility to describe precisely the spatial pattern, the phase and the amplitude of subsequent events. However, there is still a possibility to predict average intraseasonal amplitude for a particular region or a tendency for the patterns for a particular year. The relation between the ENSO phase and the ISO variance over the Indo-Pacific region gives an evident example of such predictability. During boreal winter, the MJO-like convective perturbation is indeed observed to extend eastward in El Niño years (e.g. Woolnough et al, 2000). A correct seasonal prediction of ENSO amplitude is thus expected to give also information on some ISO characteristics for the coming season.

One possibility to look at the predictability of the ISO is to consider the average OLR ISO variance (15 to 90 days) over a given area. The percentage of variance extracted from the LMA computation will give additional information on the large-scale organization of the OLR ISO perturbations. We will consider here the Indian Ocean basin (30°N-20°S; 40°E-110°E) for the May hindcasts. The ISO variance and percentage of variance of the first CEOF is computed for 90-day time sections every 5 days over the full hindcast time series (180 days from the 1st May) augmented by 120 days of ERA40 reanalysis prior to the hindcast. The corresponding observed 300-day NOAA OLR time series is used as a reference. We have thus a series of 41 points — between February 2 and September 8 — describing the running ISO variance and percentage of

variance on 90-day time sections for each member, each model and each year. This can be compared to the equivalent 41-point series constructed from observed NOAA OLR.

6.1.1. Average seasonal evolution of the OLR ISO Variance (OIV)

It is interesting to look first at statistics of the seasonal evolution of the OLR ISO variance (OIV) in the hindcasts. The evolution of the average OIV over all members and years is shown on the left side of Fig. 16 for each selected models (LODY and CNRM are not shown since they are very similar to SCWC and CRFC respectively), for NOAA OLR and for the ERA40 OLR. The observed peak of OIV is obtained in May-June, in agreement with the known seasonal evolution of the OIV over the Indian Ocean region (Bellenger and Duvel, 2007). SCWC slightly underestimate the OIV while other models tend to overestimate it. This overestimate gives a spurious maximum near the 1st June due to (i) the mixing of ERA40 and model OIV inside the same 90-day time section that lower the amplitude before the 1st June and (ii) a decrease of the OIV during the hindcast that may be related in part to observed (i.e. due to valid geophysical processes) decreasing of the OIV and in part to a convergence toward a climatological state of the models in which the OIV is underestimated.

The variance percentage (VP) characterizes the large-scale organization of the convective (OLR) perturbation and the persistence of the structure of this perturbation in the 90-day time section (see Goulet and Duvel, 2000). The observed average VP tends to be maximal in May, corresponding to bogus monsoon onset in the south Bay of Bengal (Duvel and Vialard, 2007; Bellenger and Duvel, 2007). ERA40 tends to underestimate VP in April, giving also an underestimate for the model series. Most models give correct estimate of VP. The VP is smaller for CRFC hindcasts showing a lack of organization at the intraseasonal time-scale. SMPI hindcasts have very high VP in May and June. This is related to spurious perturbations in the western Indian Ocean (see previous sections) due to a discontinuity in the OLR field between ERA40 and SMPI the 1st May. This is due to the particular computation of the initial conditions for the SMPI hindcast (coupled simulations relaxed toward observed SST up to the start of the free coupled simulation of the hindcast). In this particular case, our extension of the time series prior to the simulation using ERA40 OLR is not well adapted. It should have been better to use the time series from the relaxed SMPI run. Note however that the transition between the relaxed simulation and the free coupled run may give a spin-up of the ocean model at the intraseasonal time-scale, giving also spurious intraseasonal events at the beginning of the hindcast.

6.1.2. Spatial distribution of the OIV in the models

By looking only to 90-day time sections centered between 15 June and 8 September, one can study the spatial distribution of the OIV and of the VP related to model variability only (i.e. there is no more ERA40 information in the 90-day time sections). The regional VP is obtained by dividing the variance of the filtered input signal by the variance of the Local Mode (Eq.6). The OIV maps (Fig. 17) give some information on the origin of the value of the OIV in the different models. For the CRFC model, the large OIV is mostly related to a wide spread of the regional distribution of the OIV. For SCNR, the large OIV is related both to stronger regional values and to the regional spread. For the three other models, the value of the OIV and its regional spread is relatively correct.

The difference between observed and modeled VP is large (Fig. 18). One can first notice the larger spread of the VP distribution in the hindcast, confirming the lack of reproducibility in the pattern of the different ISO

events. There are two main regions of organized OLR perturbation for this season (East equatorial Indian Ocean and East Arabian Sea) in the observation. The enhanced VP over the East Arabian Sea is detectable for nearly all models, while of smaller amplitude. On the opposite, the VP over the East equatorial Indian Ocean region remains small for all models except for SCNR. For SMPI, there is still a strong variability to the west of the basin that can be related to the particular initial conditions of the ocean model.

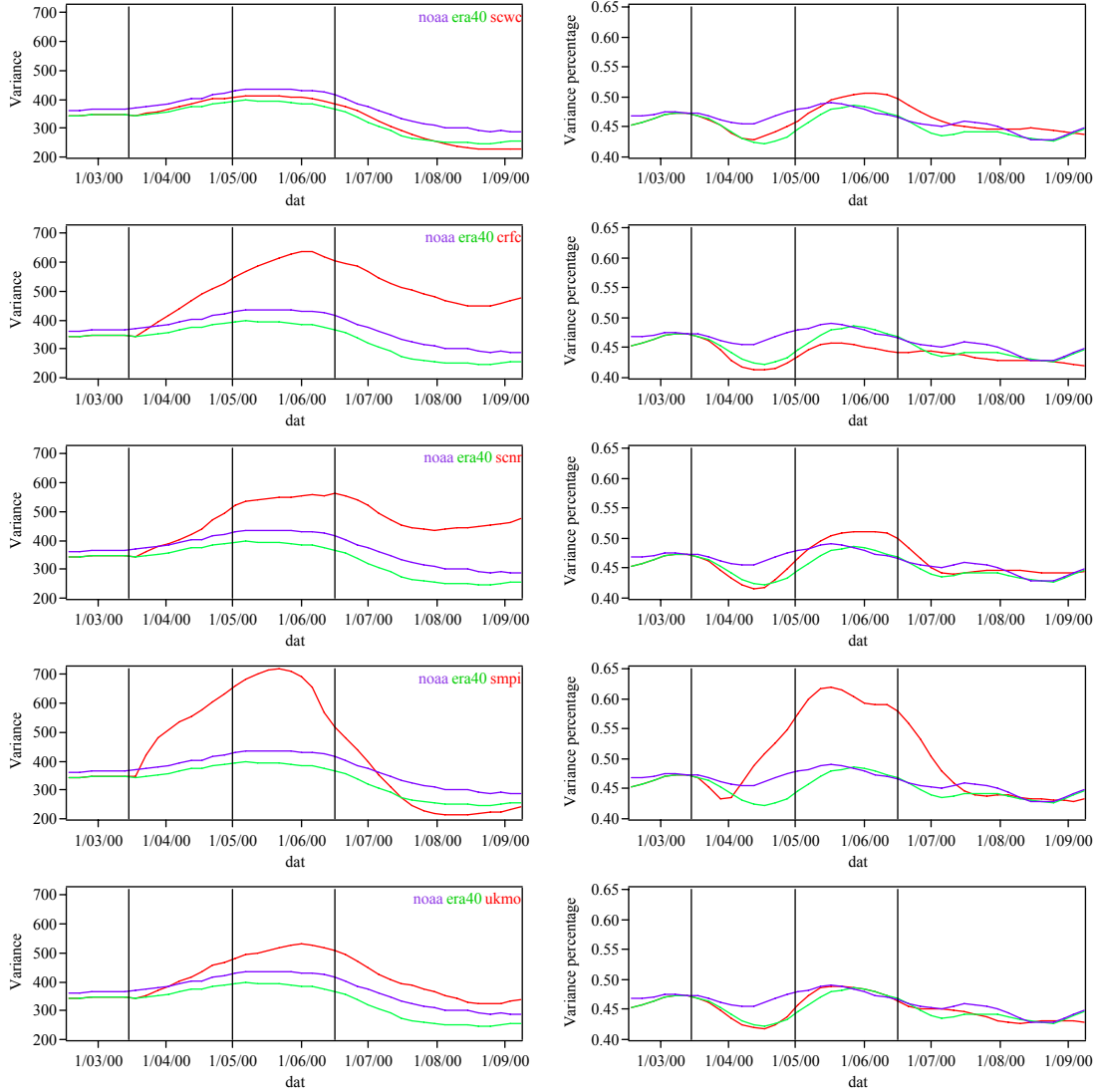


Figure 16: Average seasonal evolution of (left) the OIV over the Indian Ocean basin area (30°N - 20°S ; 40°E - 110°E) and (right) the variance percentage of the first CEOF modes. Hindcasts starting the 1st May. The total variance of the OLR (Wm^{-2}) is divided by the number of 2.5° regions in the area. The OIV is computed every 5 days on running 90-day time sections. The left vertical line is the last day with only ERA40 data in the 90-day time section, the middle one is for the beginning of the hindcast (half ERA40 and half hindcast data in the time section) and the right one the date with only hindcast data.

The spread of the OIV and the VP regional distributions in the hindcast shows that the inter-member as well as the interannual variability of the OIV could be due to variable organization of the convective perturbation at large scale. It shows that the models tend to generate ISV on various locations, while in the observation, the pattern are better established and reproducible (see also Fig. 14). By comparison, the real interannual variability of the OIV will be more related to the existence of a relatively reproducible pattern with various

amplitudes. While more debatable, this fact can also be deduced by the good correspondence between regions of both large average OIV and VP, as in the observations. If this is not the case, one may suspect the large OIV to be related more to random processes than to large-scale organized atmospheric perturbations.

6.1.3. Interannual and inter-member variability of the OIV

The interannual variability of the OIV is reported in figure 19. As for the OIV itself, the interannual variability is underestimated in the ERA40 reanalysis. For the hindcasts, we separate the average inter-member variability (standard deviation computed for each year and then averaged), the total variability (i.e. inter-member + interannual standard deviation) and the interannual variability of the ensemble mean. The difference between the inter-member and the total variability is due in part to the statistic (there is the same stochastic part between two members of two different years and two members of the same year for long coupled simulations) and in part to the initial (mostly ocean) conditions. The total variability should thus converge toward the inter-member variability near the end of the hindcasts when the simulation tends to converge toward the climatological state of the model.

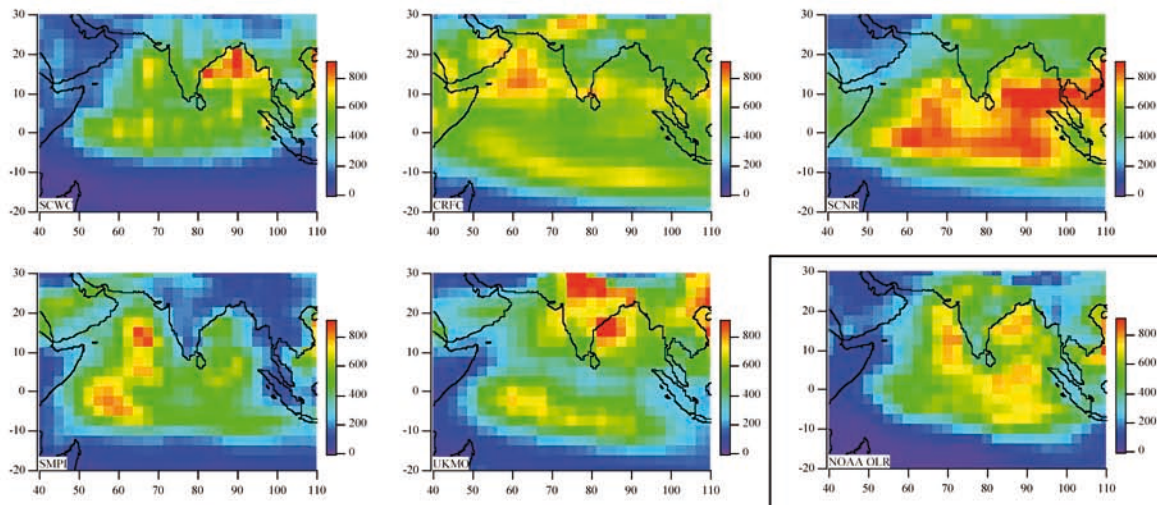


Figure 17: Average OIV for 90-day time sections centered between 15 June and 8 September.

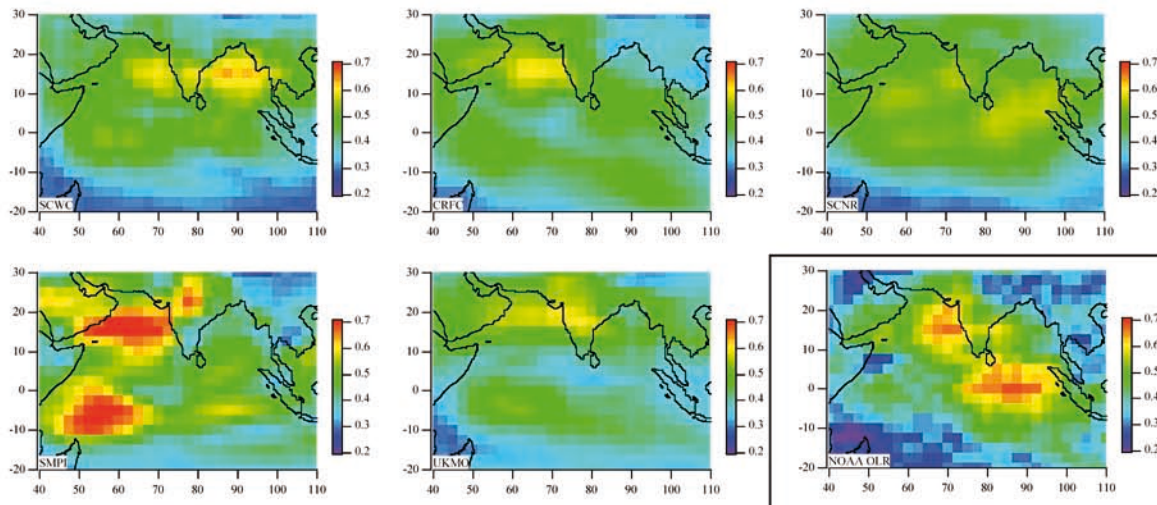


Figure 18: Average regional percentage of variance of the 1st CEOF for 90-day time sections centered between 15 June and 8 September.

For coupled model simulations with no other difference than the initial conditions, interannual variability of a ensemble mean must converge toward zero (or a statistical residual depending on the number of members) toward the end of the simulation. Near the beginning of the simulation, this interannual variability is as a mixing between a “deterministic” variability related to the ocean-atmosphere initial conditions and a “stochastic” variability that is a property of the physical system. After some time, the “deterministic” part collapse and the ensemble mean will just tend to smooth out the “stochastic” process, leaving the average climatological state of the model.

Results

The total variability of the OIV is relatively large in the hindcasts of the different models and comparable to the observed interannual variability of the OIV in May and June (Fig. 19). This total variability is overestimated afterwards, in relation to the overestimated OIV for these months (Fig. 16). The models with the stronger total and inter-member variability (CRFC and SCNR on Fig. 19) are indeed the models having the stronger average OIV (Fig. 16) and the stronger regional spread of the OIV (Fig. 17). This spread will indeed potentially increase the variability of the ISO pattern from one event to another and then from one member to another.

Because of the particular computation of the initial conditions for SMPI, the inter-member variability increases sharply as soon as the 90-day window includes the beginning of the hindcast in May. Excepted for SMPI, there is a progressive increase of the inter-member variability. The smaller inter-member variability near the beginning of the hindcasts is related in part to the time windowing (i.e. mixing with ERA40 OLR) and in part to the persistence of the effect of the ocean-atmosphere initial conditions (see the previous section). For most models, the maximum inter-member variability is obtained in July and then remains quasi-constant. On the basis of this diagnostic, one may thus expect a significant influence of the initial conditions on the IOV until July only for these 1st May hindcasts (i.e. less than 3 months).

The interannual variability of the member-average (IVMA) of the OIV decreases from May-June to September for most models. While this seems to fit to observations, this is also partly related to the progressive decrease of the influence of the initial conditions. However, the IVMA is also related in part to the statistical residual of the member average. This statistical residual (i.e. indetermination of a mean because of the variance of the population) may increase because of the relatively small number of members and the large inter-member variability for some models. The IVMA thus tends to increase as the inter-member variability increases, reducing the negative tendency related to the declining influence of the initial conditions. Prior to June15, the IVMA is also related to the observed interannual variability because of the mixing with ERA40 values. There are also large differences between models. For example, the IVMA and the inter-member variability are similar for SCWC. On the opposite, the IVMA is small compared to the inter-member variability in CRFC and SCNR.

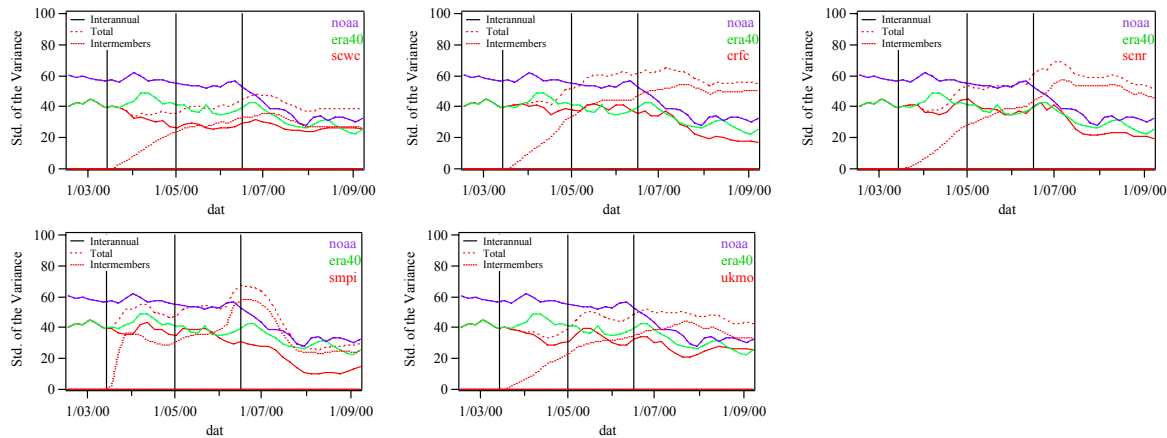


Figure 19: Total, interannual (for the ensemble mean) and inter-member (for a given year) standard deviation of the OLR ISO variance (Wm^{-2}) $_2$ for the Indian Ocean basin area (30°N - 20°S ; 40°E - 110°E) for the May hindcasts. The inter-member standard deviation is the average over the 22 years (1980-2001).

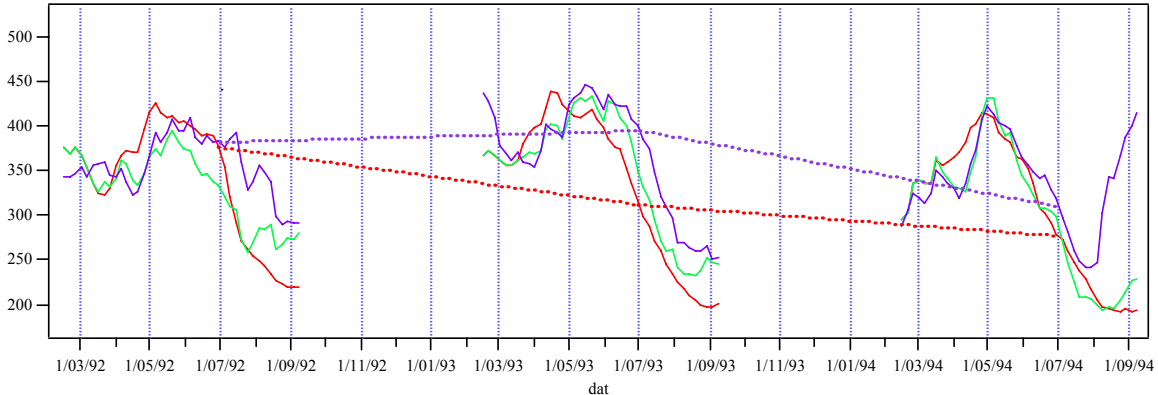


Figure 20: Evolution of the OLR ISO variance (Wm^{-2}) $_2$ during three hindcasts for the LODY model (red), ERA40 reanalysis (green) and the NOAA OLR (purple). The dotted lines represent the interannual evolution of the ISO variance for the 90-day time sections centered on the 1st July for the NOAA OLR and the LODY model.

6.1.4. Predictability of the OIV

The evolution of the ISO variance over a given area may be used to study the predictability of the intraseasonal activity. For each year, we know the seasonal evolution of the observed NOAA OLR ISO variance and the member-average (or even multi-model average) evolution during the hindcast as described above. At a given date (say 1st July), we thus know the interannual variation of the ISO variance in the corresponding 90-day time section for both observation and model. This interannual evolution is illustrated on Fig. 20 for three years for the LODY model. For the seasonal predictability, we are interested in the dotted lines that represent the interannual evolution of the ISO variance for a time section centered on a particular date (here the 1st July.) The correlation between the purple and the red dotted time-series (with 22 points corresponding to the 22 years considered) is a measure of the ability of the hindcasts to predict the ISO variance over the Indian basin for a time section between roughly June 15 and September 15 (time section centered on the 1st July). Such a correlation may be computed for each of the 41 points of OIV time series described above and represented for three years on Fig. 20 for NOAA OLR, ERA40 and the member average.

For a particular date, the 22 points corresponding to the 22 years can be considered independent, the degrees of freedom is thus 21 and a correlation of 0.53 (0.42) is significant at the 99% (95%) level. The interannual correlation is shown on figure 21 for each hindcast and for ERA40 OLR. The ERA40 OLR gives a reference for typical correlation that can be obtained with a model describing well the interannual variation of dynamical field and other observed prognostic variable. The correlation is not perfect since the OLR is computed by the model a few time steps after the data assimilation. This OLR thus strongly depends on the model parameterization. The correlation obtained with the hindcast first decreases rapidly as the 90-day window incorporates more simulated values and less ERA40 OLR value. However, most models give a subsequent increasing correlation in May and June. The multi-model average gives a correlation close to ERA40 values near June 15. The correlation then decreases rapidly towards the end of the hindcast. This shows that there is some predictability of the IOV for around 1-2 months after the beginning of the hindcast. The date of the maximum correlation also corresponds to: (i) the date of the maximum simulated ISO variance (Fig. 16); (ii) the date of a secondary maximum in the observed interannual variance (Fig. 19). In fact the date of the maximum correlation also corresponds to the date for which the OIV is computed in a 90-day time section containing hindcast output only. The lower correlation before this date can be attributed mostly to the mixing between ERA40 OLR and hindcast OLR in the same time section. There are indeed large discrepancies between these fields (Fig. 16). There is also apparently more difficulties to simulate the OLR during the period between April and June, as shown by the lower correlation obtained with ERA40. This may be related to the difficulty to represent the OLR ISO perturbations related to onsets and bogus onsets during this period. The decreasing correlation in the hindcasts during July and August shows a total lack of prediction of the ISO amplitude after 2-3 months.

Some models (CRFC, SMPI) have better prediction skill despite their poor representation of the ISO pattern. The stronger percentage of variance in the Arabian Sea could be the source for this good representation of the interannual variation of the OIV in June. The OIV is indeed maximal in June in the Arabian Sea in relation with the monsoon onset. On the opposite, SCNR does not perform well despite its better representation of the ISO pattern.

The same analysis can be done considering the amplitude of the mode (i.e. the variance of the 1st CEOF for each 90-day time section) instead of the total OIV. An improvement of the correlation means that the interannual evolution of the part of the OIV that is organized at large-scale is better simulated than the total OIV. The interannual correlation is improved for the ERA40 OLR simulations, especially in May-June (Fig. 21). This means that the assimilation of large-scale organized thermodynamic and dynamic structure makes the model able to depict the corresponding amplitude of the organized convective perturbation (and thus the organized OIV).

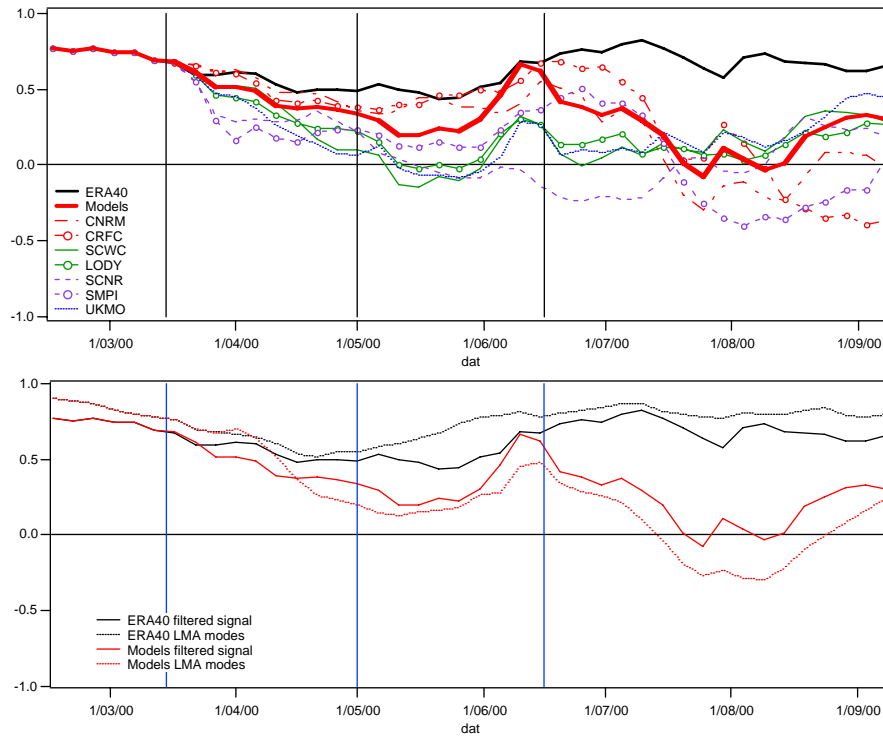


Figure 21: (Top) Time evolution of the correlation between the observed and the simulated (member average) interannual variations of the OIV. One correlation is computed every five days. The OIV is computed on a 90-day time section. (Bottom) Comparison with the same computation done on the basis of the variance of the 1st CEOF of the 90-day time section.

On the opposite, considering the amplitude of the mode instead of the total OIV decreases the interannual correlation for the models (Fig. 21). The increased correlation near the 15th June is thus not related specifically to the large-scale organized convective perturbations. This is not surprising if one consider the relatively poor representation of the pattern of the organized intraseasonal perturbations in the models.

6.2. Predictability of the intraseasonal activity (Boreal Winter)

The same analyses are performed for the November hindcasts for the same Indian Ocean basin (30°N-20°S; 40°E-110°E). The comments are limited in this section since many features are similar to the boreal summer case.

6.2.1. Average seasonal evolution of the OLR ISO Variance (OIV)

The OIV of ERA40 tends to be only slightly too small (compared to summer) at the beginning and the end of the hindcast (Fig. 22). The OIV is even slightly larger for 90-day time sections centered near the beginning of the simulation. On the opposite, the VP tends to be smaller than observation between December and March, showing a difficulty for the analysis system to organize the convection at large scale despite the assimilation of thermodynamic and dynamic observations. The observed VP tends to increase during the hindcast period, with a maximum in January-February.

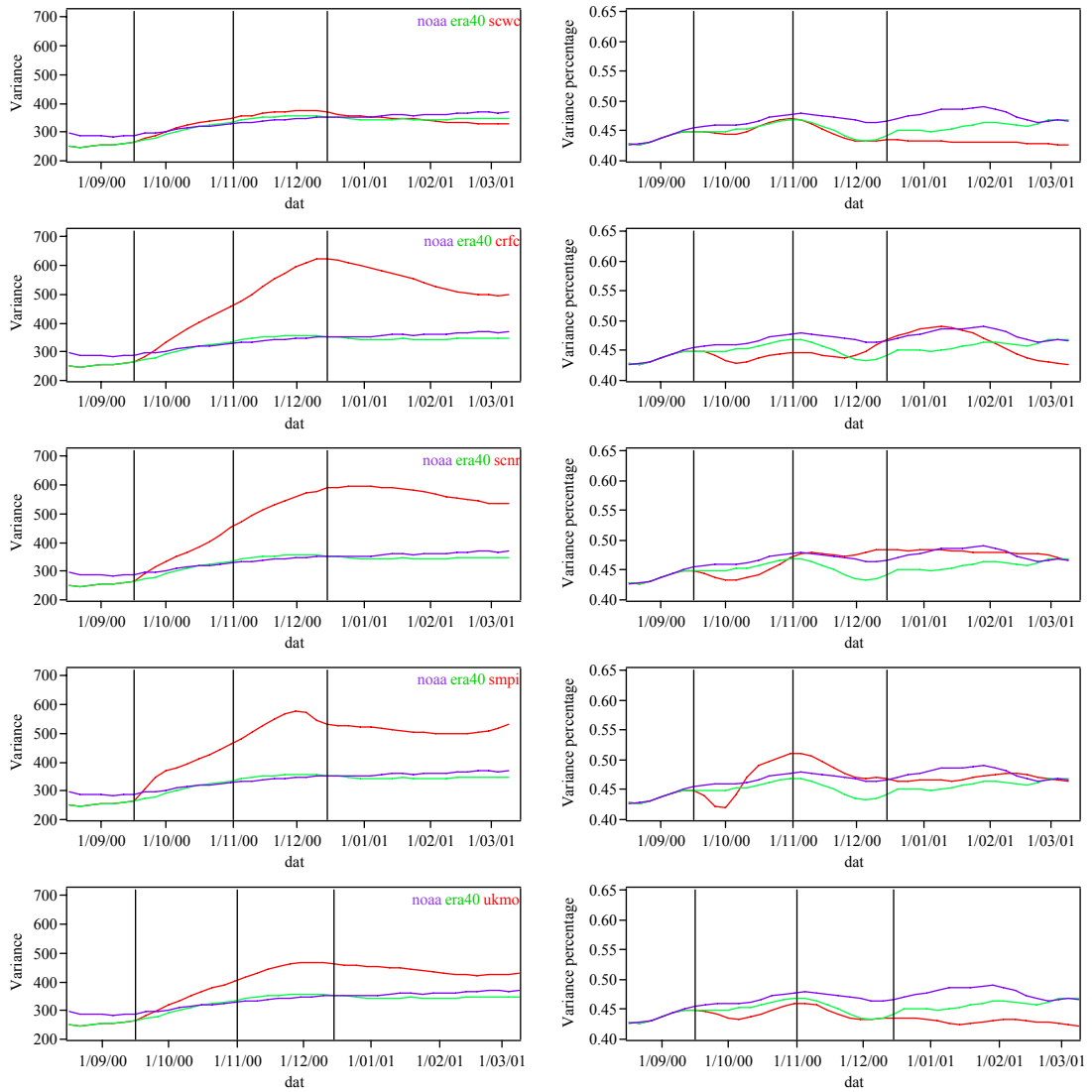


Figure 22: As Fig. 16 but for the November hindcasts

As for the May hindcasts, the OIV is overestimated for most DEMETER coupled models. The VP is particularly small for the SCWC and UKMO models for the beginning of the year. The evolution of the VP is relatively well represented for the other models, particularly after mid-December, when the 90-day time sections are representative of the coupled model only. Note the already mentioned problem in SMPI due to the computation of the initial conditions that is not well compatible with our analysis.

6.2.2. Spatial distribution of the OIV in the models

As for the boreal summer, there is a wide spread of the OIV (Fig. 23) explaining part of the overestimated OIV by the models shown in the previous section (another part may be linked to problems in the computation of the OLR in relation with the cloud parameterization). For SCWC and UKMO, the visible artifacts are likely due to the projection of the model grid onto the regular 2.5° grid. As already shown in previous sections, the maximum OIV is misplaced in the winter hindcasts. The main drawbacks are: A too longitudinally elongated region of activity (instead of the clear maximum to the East in the observation); too

large OIV in the northern hemisphere (Tip of India, south Bay of Bengal); a south position of the OIV maximum, especially for UKMO.

As for the May hindcasts, the distribution of the variance percentage (Fig. 24) shows also a too spread distribution (i.e. a lack of contrast between minima and maxima). Only SCNR gives a clear maximum VP in the East of the equatorial Indian Ocean. For SCNR, as for the May hindcasts, there is a very different spatial distribution of the OIV and the VP. In fact, the VP is maximal in between the regions of strong OIV, showing that this strong OIV is not associated with large-scale organized convective perturbations. For the UKMO winter hindcasts, the VP associated with the strong OIV maximum in the Bay of Bengal is also small.

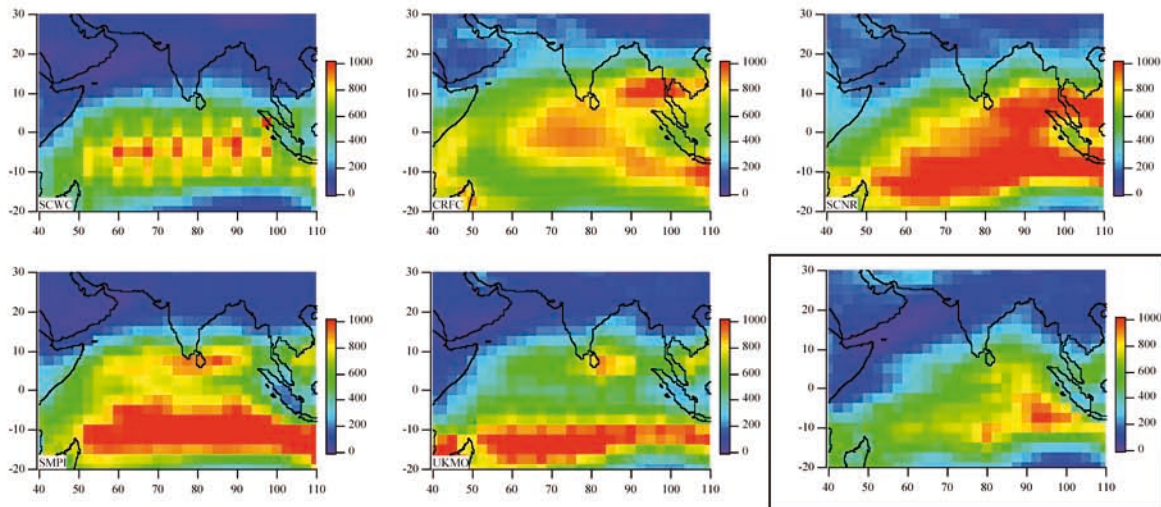


Figure 23 : As Fig. 17 but for the November hindcasts

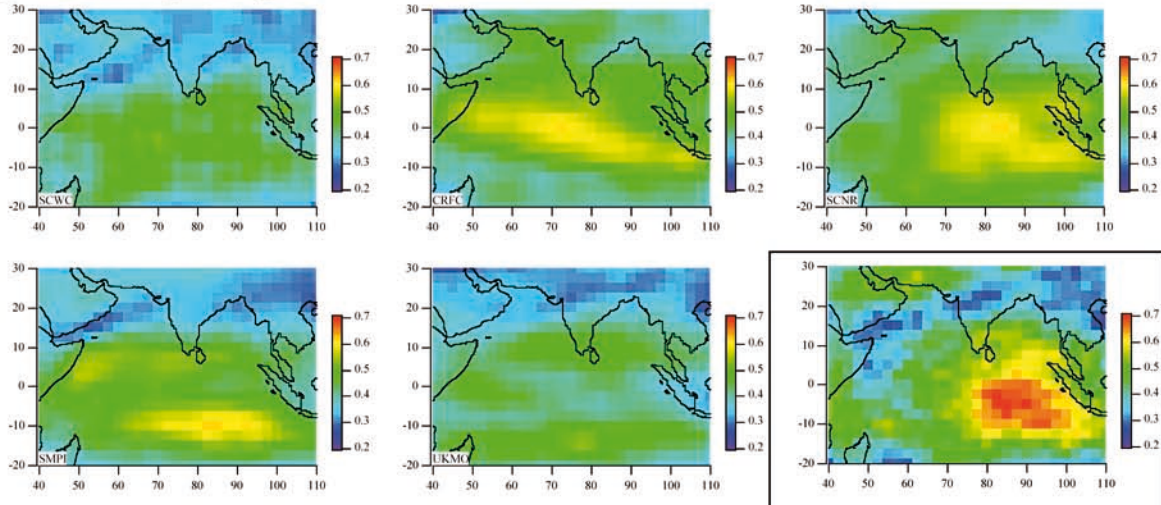


Figure 24 : As Fig. 18 but for the November hindcasts

6.2.3. Interannual and inter-member variability of the OIV

Contrary to the summer hindcasts, the total variability of the OIV is relatively small in the winter hindcasts for the different models (Fig. 25). This total variability is clearly underestimated for the SCNR and the UKMO models, despite the large OIV for UKMO. For the other models, the total variability remains small

considering that the OIV itself is overestimated (Fig. 22). The maximum interannual variability of OIV in January–February is not well depicted in the hindcasts.

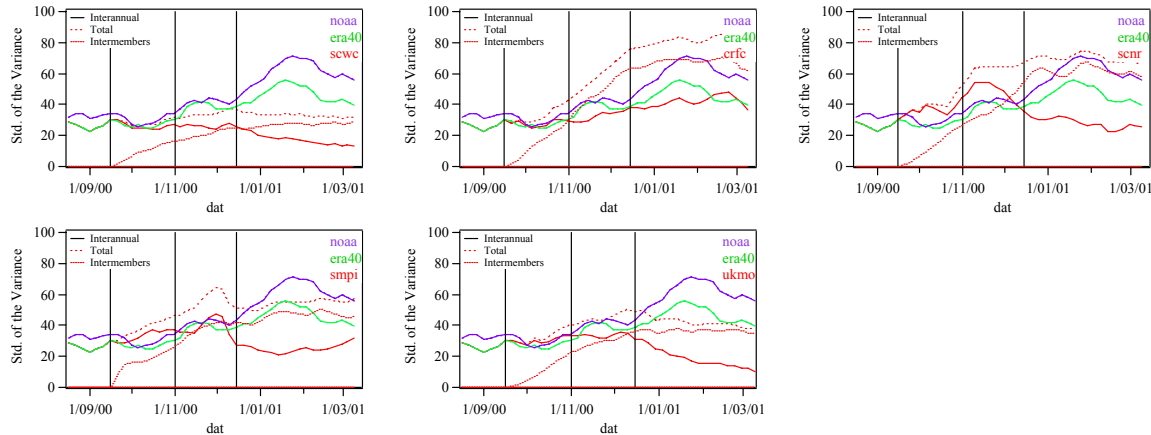


Figure 25: As Fig. 19 but for the November hindcasts

As expected, there is a progressive increase of the inter-member variability along the hindcasts (except for SMPI for reasons given above). For most models, the maximum inter-member variability is obtained in January and then remains quasi-constant. As for summer hindcasts, one may thus expect no significant influence of the initial conditions on the IOV after approximately 2 months.

The interannual variability of the member-average (IVMA) of the OIV decreases regularly for the SCWC and the UKMO models. This is not only related to the progressive decrease of the influence of the initial conditions and may be attributed to a rather fast convergence of the model toward climatological conditions. There are large differences between the three remaining models. For example, the IVMA remains high in January in CRFC, in association to large inter-member variability (there is certainly an influence of the residual of the member average). For SCNR, the inter-member variability is comparable but the IVMA is smaller.

6.2.4. Predictability of the OIV

The interannual correlation between observed and modeled IOV for the winter hindcasts (Fig. 26) follows an evolution comparable to that of summer (Fig. 21). The correlation first decreases for most models (due to the mixing with ERA40 in the same 90-day time section) and thus remains nearly constant up to December. The correlation then decreases to attain even significant negative correlation for some models. SCWC and LODY models perform better for these winter hindcasts.

In November and December, this correlation decreases if one considers the 1st CEOF of the 90-day time section instead of the total OIV. After January, the correlation using the IOV is negative and the correlation using the 1st CEOF is closer to zero.

7. Conclusion and perspectives

The study of the predictability of the tropical intraseasonal activity (or “intraseasonal oscillation” or “Madden-Julian oscillation”) in coupled models presents many difficulties. This is related to the following characteristics:

- Intraseasonal perturbations are highly intermittent with a strong seasonal variability. As a consequence, it is difficult to extract simple and significant diagnostics because of the variability of the phenomenon itself.

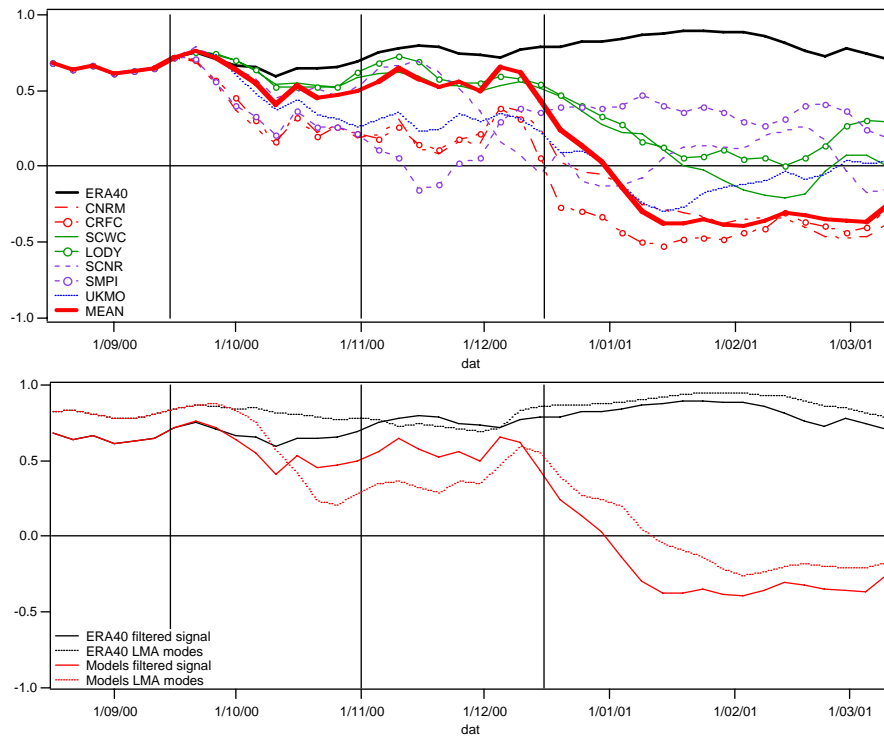


Figure 26: As Fig. 21 but for the November hindcasts

- The physics of the phenomenon is still poorly understood. In particular, the effect of the coupling between the perturbations of the deep convection and the atmospheric response (or forcing if equatorial waves are supposed to be the driving mechanism) on the intraseasonal variability is not well established. This is even complicated by the possible influence of the coupling between the convective activity and the ocean surface temperature on the fluctuation of organized intraseasonal perturbation of the deep convection. The complexity of these interactions leads to real difficulties in representing these intraseasonal perturbations in forced or coupled atmospheric models.
- There is a poor representation of the mean state and average seasonal evolution of the monsoon circulations in the coupled models. This leads to (and is certainly also partly related to) a wrong representation of the intraseasonal variability of the deep convection.

Because of these difficulties, the present analysis must be considered as a first attempt to assess the predictability of the intraseasonal activity in seasonal hindcasts. To answer the above critical points, a particular attention was given to:

- The relation between the seasonal cycle and the intraseasonal activity, especially for boreal summer when the intraseasonal activity is strongly linked to the seasonal march of the monsoon (see also Bellenger and Duvel, 2007).

- The intermittency of the phenomenon by considering distributions of the characteristics of the intraseasonal events rather than only average perturbation patterns (use of the multi-variate LMA).
- The average state of the model and, more importantly, the average seasonal evolution of the convective activity into which the intraseasonal variability is embedded.
- The evaluation of the representation of the coupling between the convection, the low-level wind and the SST at intraseasonal time scales.

A specific set of diagnostics was developed that aims to take into account these different points. Considering the ensemble of the DEMETER hindcast, we can give these preliminary conclusions.

- The multi-variate LMA shows that most models have problems in simulating large-scale organized perturbations of the convection. In addition, perturbation patterns are more variable from one intraseasonal event to another compared to observation. However, most models do exhibit some form of northeastward propagation of the perturbations over the Indian Ocean during boreal summer. Realistic periods of the modes (25-35 days) are produced in a few models, while most models produce shorter periods (20-25 days).
- Models with poor seasonal cycle tends to have larger biases in the northeastward propagation and organization boreal summer hindcasts. One possible source of deficiency in organizing intraseasonal large-scale convective perturbation could be the air-sea interaction. The analysis of the nature of coupling in the hindcasts indeed shows that most models simulate too weak SST perturbations and systematic phase quadrature between OLR and SST, indicative of a slab-ocean-like response of the temperature to surface flux perturbations. Simulation done with the same AGCM and different OGCMs tend to have similar biases of the simulated ISOs, indicative of the importance of atmospheric processes in defining the nature of the intraseasonal SST perturbation.
- Evaluation of the predictability at the ISO time scale (10-50 days) is also performed on the basis of pentad mean OLR maps. This “deterministic” predictability of the intraseasonal perturbation of the convection is better in boreal summer than in boreal winter. This is related to the marked seasonal variation that leads to a better consistency between the different members of the ensemble simulations. This enhanced predictability can possibly impact the seasonal predictability.
- Considering the potential influence of the ocean thermal structure on the amplitude of the intraseasonal perturbations of the convection, some prediction skill could results from the ocean initial conditions. An evaluation of the seasonal prediction of the mean OLR intraseasonal variance (OIV) on the Indian Ocean basin was performed on the basis on the evolution of this OIV in running 90-day time sections. Results show no particular skill to predict the OIV for the coming season (after two months of hindcast). Intriguing maxima in the interannual correlation between observed and simulated values is nevertheless obtained for the OIV during the first 90 days of the hindcast simulation. The origin of this maximum deserves further investigation.

The too systematic phase relationships between the convection and SST perturbations, and the relatively small SST perturbations, are indicative of the limited capabilities of the ocean models to simulate SST

perturbations. This may be due to surface processes such as warm layer formation that is not simulated with current OGCM because of the poor vertical resolution. The relatively small perturbation of the SST may be also related to underestimated surface turbulent and radiative fluxes perturbations given by the atmospheric models. This limits the perturbation of the ocean mixed layer temperature and may also generate insufficient mixing between the mixed layer and the deeper ocean during strong surface wind phase.

All these process will be studied in more detail in a near future. Studies are also in progress with an emphasis on the influence of large-scale organized ISO perturbations on the regional seasonal evolution of the precipitation at particular location. The different approaches that have been developed here, together with new diagnostics that emerged from this preliminary analysis, will be used to assess the representation of the intraseassonal variability and its predictability in the ENSEMBLE hindcats simulations.

References

- Bellenger, H. and J.P. Duvel , 2007: Intraseasonal Convective Perturbations related to the Seasonal March of the Indo-Pacific Monsoons, *Journal of Climate*, in press.
- Bhat, G.S. et al, 2001: BOBMEX: The Bay of Bengal monsoon experiment, *Bull.Amer.Meteor.Soc.*, **82**, 2217-2243.
- De Boyer Montegut C., G. Madec, A. S. Fischer, A. Lazar, and D. Iudicone, 2004: Mixed layer depth over the global ocean: an examination of profile data and a profile based climatology, *J. Geophys. Res.* **109**, C12003, doi:10.1029/2004JC002378.
- Duchon, C.E., 1979: Lanczos filtering in one and two dimensions, *J.Appl.Meteor.*, **118**, 1016-1022.
- Duvel, J-P. and J. Vialard, 2007: Indo-Pacific sea surface temperature perturbations associated with intraseasonal oscillation of the tropical convection. *J. Climate* (in press)
- Duvel, J-P., R. Roca and J. Vialard, 2004: Ocean Mixed Layer Temperature Variations induced by Intraseasonal Convective Perturbations over the Indian Ocean. *J. Atmos. Sci.*, **61**, 1004-1023.
- Fennessy, M., and J. Shukla, 1994: Simulation and predictability of monsoons. Proceedings of the international conference on monsoon variability and prediction, WMO/TD 619, Trieste, Italy, pp. 567–575.
- Ferranti, L., J. M. Slingo, T. N. Palmer, and B. J. Hoskins, 1997: Relations between interannual and intraseasonal monsoon variability as diagnosed from AMIP integrations. *Quart. J. Roy. Meteor. Soc.*, **123**, 1323–1357.
- Flatau, M., P. J. Flatau, P. Phoebus, and P. P. Niiler, 1997: The feedback between equatorial convection and local radiative and evaporative processes: The implications for intraseasonal oscillations, *J. Atmos. Sci.*, **54**, 2373-2386.
- Flatau, M. K. , P. J. Flatau and D. Rudnick. 2001: The Dynamics of Double Monsoon Onsets. *J. Climate*, **14**, 4130–4146.

- Fu, X., B. Wang, T. Li, and J. P. McCreary, 2003: Coupling between northwardpropagating, intraseasonal oscillations and sea surface temperature in the Indian Ocean. *J. Atmos. Sci.*, **60**, 1733–1753.
- Fu, X., B. Wang, D. E. Waliser, and T. Li, 2007: Impact of atmosphere-ocean coupling on the predictability of monsoon intraseasonal oscillations (MISO). *J. Atmos. Sci.*, p. in press.
- Gadgil, S., and S. Sajani, 1998: Monsoon precipitation in the AMIP runs. *Climate Dyn.*, **14**, 659–689.
- Gill, A. E., 1980: Some simple solutions for heat-induced tropical circulation. *Quart. J. Roy. Meteor. Soc.*, **106**, 447–462.
- Goswami, B. N., 2005: South Asian monsoon. Intraseasonal variability in the Atmosphere-Ocean climate system, K. Lau and D. Waliser, Eds., Praxis. Springer Berlin Heidelberg, pp. 19–61.
- Goswami, B. N., and R. S. Ajayamohan, 2001: Intraseasonal oscillations and interannual variability of the Indian summer monsoon. *J. Climate*, **14**, 1180–1198.
- Goswami, B. N., and P. K. Xavier, 2003: Potential predictability and extended range prediction of Indian summer monsoon breaks. *Geophys. Res. Lett.*, **30**(18)(1966), doi:10.1029/2003GL017,810.
- Goswami, B. N., and P. K. Xavier, 2005: Dynamics of ‘internal’ interannual variability of the Indian summer monsoon in a GCM. *J. Geophys. Res.*, **110**(D24104), doi:10.1029/2005JD006,042.
- Goulet, L., and J-P. Duvel, 2000: A new approach to detect and characterize intermittent atmospheric oscillations: Application to the intraseasonal oscillation. *J. Atmos. Sci.*, **57**, 2397–2416.
- Kang IS, K. J. Wang B, Lau KM, Shukla J, Schubert SD, Waliser DE, Krishnamurthy V, Stern WF, Satyan V, Kitoh A, Meehl GA, Kanamitsu M, Galin VY, Kim JK, Sumi A, Wu G, Liu Y (2002) Intercomparison of the climatological variations of Asian summer monsoon precipitation simulated by 10 GCMs. *Clim Dyn.*, **19**, 383-395.
- Kemball-Cook S., and B. Wang, 2001: Equatorial waves and air-sea interaction in the boreal summer intraseasonal oscillation. *J. Climate*, **14**, 2923–2942.
- Kemball-Cook, S., B. Wang, and X. Fu, 2002: Simulation of the Intraseasonal Oscillation in the ECHAM-4 Model: The Impact of Coupling with an Ocean Model, *J. Atmos. Sci.*, **59**, 1433-1453.
- Lengaine, M., et al., 2002: Ocean response to the March 1997 westerly wind event, *J. Geophys. Res.*, **107**(C12), 8015, doi: 10.1029/2001JC000841.
- Liebmann, B., and C. A. Smith, 1996: Description of a complete (interpolated) outgoing longwave radiation dataset. *Bull. Amer. Meteor. Soc.*, **77**, 1275–1277.
- Lo, F., and H. H. Hendon, 2000: Empirical extended-range prediction of the Madden-Julian oscillation. *Mon. Wea. Rev.*, **128**, 2528 2543.

- Madden, R. A., and P. R. Julian, 1994: Observations of the 40-50 day tropical oscillation: A Review, *Mon. Wea. Rev.*, **122**, 813-837.
- Maloney, E.D. and A. H. Sobel. 2004: Surface Fluxes and Ocean Coupling in the Tropical Intraseasonal Oscillation. *J. Climate*, **17**, 4368–4386.
- McPhaden, M. J., 1999: Genesis and evolution of the 1997 1998 El Nino. *Science*, **283**, 950 954.
- Palmer, T. N., et al., 2004: Development of a European multimodel ensemble system for seasonal-to-interannual prediction (DEMIETER). *Bull. Amer. Meteor. Soc.*, DOI: 10.1175/BAMS-85-6-853.
- Reynolds, R. W., and T. M. Smith, 1994: Improved global sea surface temperature analyses using optimum interpolation. *J. Climate*, **7**, 929 948.
- Sengupta, D., and M. Ravichandran, 2001: Oscillations of Bay of Bengal sea surface temperature during the 1998 summer monsoon, *Geophys. Res. Lett.*, **28**, 2033-2036.
- Sengupta, D., B.N. Goswami, and R. Senan, 2001: Coherent intraseasonal oscillations of ocean and atmosphere during the asian summer monsoon, *Geophys. Res. Lett.*, **28**, 4127-4130.
- Slingo, J. M., et al., Intraseasonal oscillations in 15 atmospheric general circulation models: results from an AMIP diagnostic subproject, *Climate Dyn.*, **12**, 325 357, 1996.
- Sperber, K. R., C. Brankovic, M. Deque, C.S., Frederiksen, R. Graham, A. Kitoh, C. Kobayashi, T. Palmer, K. Puri, W. Tennant and E. Volodin, 2001: Dynamical seasonal predictability of the Asian summer monsoon. *Mon. Wea. Rev.*, **129**, 2226-2248.
- van Den Dool, H. M., and S. Saha, 1990: Frequency dependence in forecast skill. *Mon. Wea. Rev.*, **118**, 128–137.
- Vecchi, G.A., and D.E. Harrison, 2002: Monsoon Breaks and Subseasonal Sea Surface Temperature Variability in the Bay of Bengal, *J. Climate*, **15**, 1485-1493.
- Waliser, D. E., W. Stern, S. Schubert, and K. M. Lau, 2003a: Dynamic predictability of intraseasonal variability associated with the Asian summer monsoon. *Quart. J. Roy. Meteor. Soc.*, **129**, 2897–2925.
- Waliser, D. E., R. Murtugudde, and L. Lucas, 2003b: Indo-Pacific Ocean Response to Atmospheric Intraseasonal Variability. Part I: Austral Summer and the Madden-Julian Oscillation, *J. Geoph. Res. - Oceans*, **108**, C5, 3160, 10.1029/2002JC001620.
- Waliser, D. E., C. Jones, C. Schemm, and N. E. Graham, 1999 : A statistical extended-range tropical forecast model based on the slow evolution of the Madden-Julian oscillation. *J. Climate*, **12**, 1918 1939.
- Wang, B., and X. Xie, 1998: Coupled modes of the warm pool climate system. Part I: the role of air-sea interaction in maintaining Madden-Julian Oscillation. *J. Climate*, **11**, 2116-2135.

- Webster, P. J., and C. Hoyos, 2004: Forecasting monsoon rainfall and river discharge variability on 15-30 day time scales. *Bull. Amer. Meteorol. Soc.*, **85**, 1745-1765.
- Webster, P.J., et al, 2002: The JASMINE Pilot study. *Bull.Amer.Meteor.Soc.*, **83**, 1603-1630.
- Wentz,F.J., C. Gentemann, D.Smith, D.Chelton, 2000: Satellite measurements of sea-surface temperature through clouds. *Science*, **288**, 847-850.
- Woolnough, S. J., J. M. Slingo, B. J. Hoskins, 2000: The Relationship between Convection and Sea Surface Temperature on Intraseasonal Timescales. *J. Climate*, **13**, 2086–2104.
- Woolnough, S. J., F. Vitart, M. A. Balmaseda, 2007: The role of the ocean in the Madden-Julian Oscillation: Implications for MJO prediction. *Quart. J. Roy. Meteor. Soc.*, **133**, 117-128
- Wu M.L.C, Schubert S., Kang I.S., Waliser D.E. (2002) Forced and free intra-seasonal variability over the South Asian Monsoon region simulated by 10 AGCMs. *J. Climate*, **15**, 2862 2880
- Zhang C., 2005: Madden Julian oscillation. *Rev. Geophys.*, **43**, RG2003, doi:10.1029/2004RG000158.
- Zhang C., M. Dong, S. Gualdi, H. H. Hendon, E. D. Maloney, A. Marshall, K. R. Sperber, and W. Wang, 2006: Simulations of the Madden–Julian oscillation in four pairs of coupled and uncoupled global models. *Climate Dyn.*, **27**, 573–592.